Geophysical Journal International

Geophys. J. Int. (2017) **208,** 748–766
Advance Access publication 2016 November 8
GJI Seismology

doi: 10.1093/gji/ggw421

Fault geometry and slip distribution of the 2008 M_w 7.9 Wenchuan, China earthquake, inferred from GPS and InSAR measurements

Yongge Wan,[1] Zheng-Kang Shen,[2,3] Roland Bürgmann,[4] Jianbao Sun[5] and Min Wang[5]

[1]*Institute of Disaster Prevention, Yanjiao, Sanhe City, Hebei Province* 065201, *China*
[2]*Department of Earth, Planetary, and Space Sciences, UCLA, Los Angeles, CA* 90095–1567, *USA. E-mail: zshen@ucla.edu*
[3]*Department of Geophysics, School of Earth and Space Science, Peking University, Beijing* 100871, *China*
[4]*Department of Earth and Planetary Science, UC Berkeley, Berkeley, CA* 94720–4767, *USA*
[5]*State Key Laboratory of Earthquake Dynamics, Institute of Geology, China Earthquake Administration, Beijing* 100029, *China*

Accepted 2016 November 7. Received 2016 November 3; in original form 2016 March 24

SUMMARY

We revisit the problem of coseismic rupture of the 2008 M_w7.9 Wenchuan earthquake. Precise determination of the fault structure and slip distribution provides critical information about the mechanical behaviour of the fault system and earthquake rupture. We use all the geodetic data available, craft a more realistic Earth structure and fault model compared to previous studies, and employ a nonlinear inversion scheme to optimally solve for the fault geometry and slip distribution. Compared to a homogeneous elastic half-space model and laterally uniform layered models, adopting separate layered elastic structure models on both sides of the Beichuan fault significantly improved data fitting. Our results reveal that: (1) The Beichuan fault is listric in shape, with near surface fault dip angles increasing from ∼36° at the southwest end to ∼83° at the northeast end of the rupture. (2) The fault rupture style changes from predominantly thrust at the southwest end to dextral at the northeast end of the fault rupture. (3) Fault slip peaks near the surface for most parts of the fault, with ∼8.4 m thrust and ∼5 m dextral slip near Hongkou and ∼6 m thrust and ∼8.4 m dextral slip near Beichuan, respectively. (4) The peak slips are located around fault geometric complexities, suggesting that earthquake style and rupture propagation were determined by fault zone geometric barriers. Such barriers exist primarily along restraining left stepping discontinuities of the dextral-compressional fault system. (5) The seismic moment released on the fault above 20 km depth is 8.2×10^{21} N m, corresponding to an M_w7.9 event. The seismic moments released on the local slip concentrations are equivalent to events of M_w7.5 at Yingxiu-Hongkou, M_w7.3 at Beichuan-Pingtong, M_w7.2 near Qingping, M_w7.1 near Qingchuan, and M_w6.7 near Nanba, respectively. (6) The fault geometry and kinematics are consistent with a model in which crustal deformation at the eastern margin of the Tibetan plateau is decoupled by differential motion across a decollement in the mid crust, above which deformation is dominated by brittle reverse faulting and below which deformation occurs by viscous horizontal shortening and vertical thickening.

Key words: Space geodetic surveys; Earthquake dynamics; Earthquake source observations; Continental dynamics: compressional; Dynamics: seismotectonics.

1 INTRODUCTION

The 2008 May 12 M_w 7.9 Wenchuan, China earthquake represents a rare major continental thrust event (Burchfiel *et al*. 2008; Klinger *et al*. 2010; Zhang *et al*. 2010). It struck the Longmen Shan fault system along the eastern rim of the Tibetan Plateau, causing more than 80 000 fatalities and about 330 000 injuries. Despite its active micro-seismicity, the largest known earthquake that occurred on the fault system in the past several hundreds of years prior to Wenchuan was merely an M6.5 event. Alongside the transpressional fault system the Longmen Shan uplifted by more than 3000 metres above the Sichuan basin, but slip rates across the faults were estimated at only about a couple of millimetres per year from field geology (e.g. Burchfiel *et al.* 1995; Densmore *et al.* 2007, 2010) and GPS (e.g. Zhang *et al.* 2004; Shen *et al.* 2005). The driving mechanism of the orogenic system and faulting deformation continue to be debated, with arguments over whether the system is dominated by lower crust channel flow or if it is the result of brittle crustal thickening and shortening (e.g. Royden *et al.* 2008; Hubbard & Shaw 2009). The fault strength and structure are also of particular interest, leading

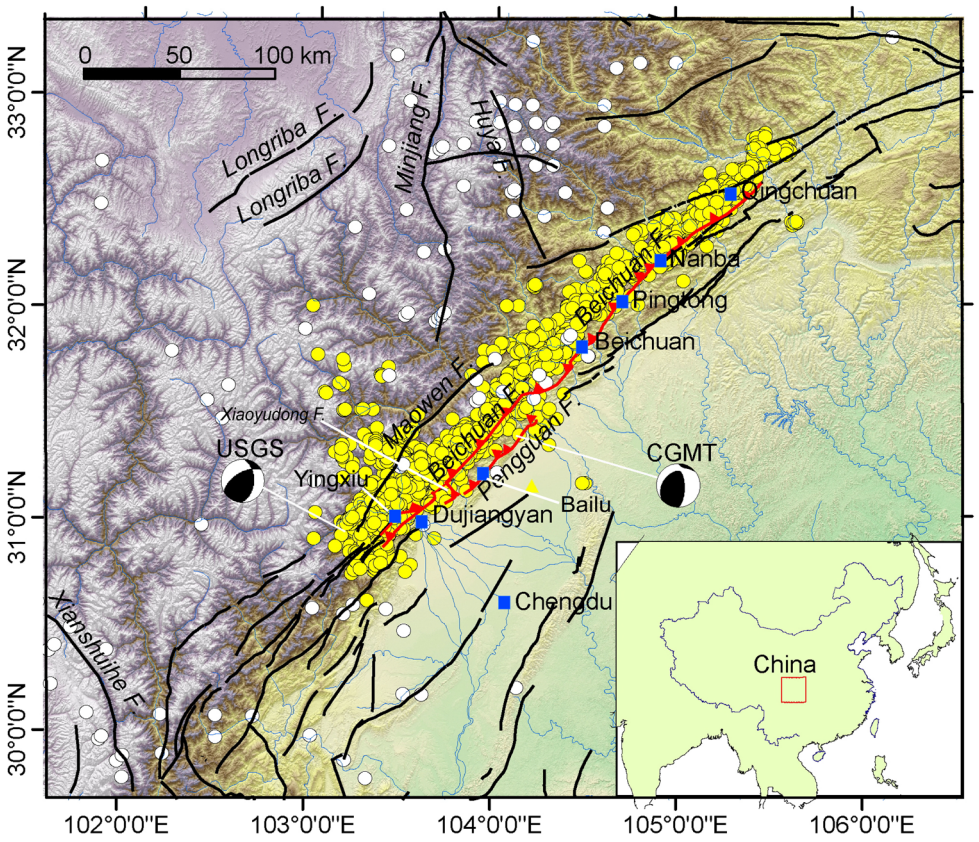

Figure 1. Tectonic setting of the Wenchuan earthquake (revised after fig. 1 of Shen *et al*. 2009). Black and red lines indicate regional faults and surface traces of coseismic rupture. Two main-shock focal mechanism solutions, USGS and CGMT, denote the microepicentre and the centroid moment tensor of event from the United States Geological Survey and the Global CMT solution, respectively. The white and yellow circles show $M > 4.7$ earthquakes of the past century and the $M > 2.0$ Wenchuan aftershocks, respectively. Blue squares denote the cities. The inset sketch shows location of the region in east Asia.

to questions as to where the strongholds (asperities or barriers) on the fault plane are located, and how these strongholds physically determine the deformation process on the fault. The Wenchuan earthquake caused substantial changes in the stress field in and around the Longmen Shan fault zone (e.g. Parsons *et al.* 2008; Toda *et al.* 2008; Wan & Shen 2010), and arguably triggered the M_w6.9 Lushan earthquake, which occurred 5 yr later on the Longmen Shan fault about 80 km southwest of the Wenchuan epicentre (Jiang *et al.* 2014). To assess earthquake potential after the quake, it is important to know how the fault system will evolve mechanically (Parsons & Segou 2014; Wang *et al.* 2014b). To address all these questions, it is essential to acquire the most detailed and accurate description of the Wenchuan rupture, including its fault geometry and slip distribution.

The Wenchuan earthquake ruptured two subparallel faults (Liu-Zeng *et al.* 2009; Xu *et al.* 2009). The Beichuan (also known as the Yingxiu-Beichuan) fault and the Pengguan (also known as the Guanxian-Jiangyou or Hanwang) fault are regarded as the central and mountain-frontal faults of the Longmen Shan fault system, striking northeasterly and separating the Songpan-Ganzi block at the eastern rim of the Tibetan plateau from the Sichuan basin (Fig. 1). The surface breaks along the Beichuan fault are found to be about 240 km long (Xu *et al.* 2009). The aftershocks, however, extend the rupture zone about 30 and 50 km beyond the southwest and northeast ends of the surface rupture trace, respectively. The Pengguan fault is located about 12 km southeast of the Beichuan fault. The surface breaks along the Pengguan fault were measured over a ~72 km distance. The conjugate Xiaoyudong fault strikes northwesterly and offsets the Beichuan fault with a left step of about 4 km. The Xiaoyudong fault ruptured coseismically, with metre-level left-slip at the surface, and the southeast end of its surface break is connected with the southwest end of the surface rupture of the Pengguan fault (Xu *et al.* 2009; Fig. 1).

The slip distribution of the Wenchuan earthquake has been investigated extensively. Numerous studies reported on the surface offsets of the coseismic rupture (e.g. Xu *et al.* 2008, 2009; Lin *et al.* 2009; Liu-Zeng *et al.* 2009; Zhang *et al.* 2010), and showed maximum reverse faulting near Hongkou (~6 m) and Beichuan (~7–10 m). Slip distributions inverted using teleseismic data demonstrated similar rupture pattern, but the depth distribution of peak slip varied markedly, ranging from near the surface to below 10 km depth (Ji & Hayes 2008; Nishimura & Yagi 2008; Wang *et al.* 2008; Zhang *et al.* 2009a; Nakamura *et al.* 2010; Zhang *et al.* 2011). Geodetic studies using GPS and InSAR data also estimated the slip distribution, and showed results overall similar to that of seismic studies but favour peak slip at shallower depth (Hao *et al.* 2009; Hashimoto *et al.* 2009; Shen *et al.* 2009; Feng *et al.* 2010; Tong *et al.* 2010; Xu *et al.* 2010; Wang *et al.* 2011; Fielding *et al.* 2013). The three kinds of studies, although differing in various details, agree on two maximum slip peaks near Hongkou/Yingxiu and Beichuan, with dominant reverse faulting along the southwest segment and dextral slip along the northeast segment of the fault rupture. Some studies also detected slip concentrations near Qingping and Nanba, but with smaller amplitudes than that of the two peak slip zones (e.g. Feng *et al.* 2010; Xu *et al.* 2010). Wang *et al.* (2011), using InSAR data and a GPS data set with much denser spatial coverage than all of

the previous studies, inverted the slip distribution in greater details. Their slip inversion identified two separate slip peaks at Hongkou and Yingxiu, a peak at shallow depth near Beichuan, a slip concentration at depth underneath Qingchuan, and a couple of high-slip regions on the decollement interface downdip of a fault ramp west of the surface rupture. Another study by Fielding *et al*. (2013) considered teleseismic waveforms, GPS displacements, InSAR and image offset data, and obtained a coseismic slip distribution that is similar to that of Wang *et al*. (2011).

Despite of the general consensus on the overall fault rupture distribution, there are still a number of outstanding questions, which have not been well addressed. One of these issues is fault geometry. It is well recognized that the fault geometry of the Wenchuan earthquake is rather complex. The Beichuan fault is found to dip steeply at numerous spots on the surface, but how the dip angle varies along strike and particularly downdip is not well known. Geological and seismic reflection studies suggest that the Beichuan and Pengguan faults are listric in shape and imbricated within the upper crust, but rooted together into a detachment at mid to lower crustal depths (Jia *et al.* 2006, 2010; Xu *et al.* 2009; Zhang *et al.* 2009b; Li *et al.* 2010; Feng *et al.* 2016). Precisely relocated aftershocks show that the hypocentre locations are widely spread across the southwest segment but narrowly distributed along the northeast segment of the fault system, implying a shallower fault dip in the southwest and steep dips along the northeast segment of the fault (Huang *et al.* 2008; Zhu *et al.* 2008; Chen *et al.* 2009). Most of the seismological studies on the rupture process adopted a fixed fault geometry based on geological and/or focal mechanism data; with a few exceptions which explored a limited part of the parameter space of fault geometry in their model inversions. Several geodetic studies attempted solving for fault geometry; for example, Shen *et al*. (2009) inverted for a fault rupture with piece-wise continuously varying fault dip, and Furuya *et al*. (2010) estimated variable dip angles of the major fault segments in their model. Fielding *et al*. (2013) also determined optimal fault dip angles for multiple Beichuan fault segment as well as the Pengguan fault. Although results from these studies share a common overall pattern, they differ in many details and yield about 10°–20° discrepancies for most of the dip angle estimates of the fault segments.

Studies by Jia *et al.* (2006, 2010), using seismic reflection data, deduced crustal structure along several profiles across the fault system. Their results illustrate about 45° dip for the Beichuan fault near the surface and about 35° dip for the Pengguan fault along a profile near Bailu (Fig. 1). A similar result was also obtained by Xu *et al*. (2009) using the same data set. The lack of data observed further west of the Beichuan fault prevented them from observing the Beichuan fault geometry further downdip. The crustal structure along two profiles across the northeast segment of the earthquake rupture seemed to suggest rather gently dipping strata and the fault interface dipping to the northwest at ∼20° (Jia *et al.* 2010; Li *et al.* 2010). Such a result seems to be quite controversial because it is in direct contradiction with geodetic inversions and the distribution of aftershocks (e.g. Huang *et al.* 2008; Chen *et al.* 2009; Shen *et al.* 2009), and may not be illustrative of the Beichuan fault but of tilted and inactive geologic structures (Li *et al.* 2010).

Another concern involved with most of the geodetic studies for fault rupture modelling is that they usually assume deformation in a homogeneous elastic half-space, ignoring vertical changes of earth media and lateral differences of elastic material properties across the Longmen Shan fault zone (e.g. Hashimoto *et al.* 2009; Feng *et al.* 2010; Tong *et al.* 2010). Ignoring the layered structure of the crust can result in up to 15 per cent of errors for deformation modelling such as for the amount and location of slip at depth (e.g. Savage 1987; Wald & Graves 2001). Wang *et al*. (2011) tested a model employing the CRUST-2 model structure, a global layered crustal model (Bassin *et al.* 2000) for computing the Green's functions, but obtained no improvements on model fitting, possibly due to mismatch of the model with the regional crustal structure. Seismic studies also demonstrate significant lateral differences of crustal structure (up to 10–15 per cent in seismic velocities) between the Sichuan basin and Songpan-Ganzi block across the Longmen Shan fault system (Huang *et al.* 2003; Wang *et al.* 2007; Zhang *et al.* 2009b; Xu & Song 2010), and neglecting such a difference could also result in biases of modelling results (Du *et al.* 1994; Williams & Wallace 2015).

In this paper we develop a coseismic slip model constrained using GPS and InSAR data, with particular effort made toward estimating the 3-D geometry of the fault rupture. A model of listric fault geometry is considered, which is allowed to vary continuously along strike. Two sets of layered earth models are employed on either side of the fault rupture for Green's function computation to account for the lateral contrast of the layered models across the fault. Our final result presents a model of slip distribution and fault geometry, which satisfactorily interprets the geodetic data and agrees well with the surface geology and general pattern of aftershock distribution.

2 InSAR, GPS, LEVELLING AND TRIANGULATION DATA

InSAR, GPS and levelling coseismic displacement data are used as model constraints in this study. The InSAR data are from observations of JAXA's ALOS and ESA's Envisat satellites. The data are from three sources: (1) the interferograms from Shen *et al*. (2009), which include eight ALOS LOS interferograms derived from repeated SAR measurements (observed 0.2–1.4 yr before and 1–7 weeks after the quake) along ascending paths 470–477 (Figs 2a and b). The southern portions of tracks 471, 472 and 476 and the northern portion of track 473 of ALOS data are affected by severe ionospheric disturbances (delineated within black outlines in Fig. 2) and have been removed prior to the slip inversion. Another LOS interferogram was derived from SAR data of Envisat descending track 290, covering a portion of near-field coseismic deformation on the footwall side of the fault (Fig. 2c). (2) The LOS interferograms from Fielding *et al*. (2013), which include data from the Envisat descending tracks of 333, 061, 018 and 247 (Figs 2d and f) and the ALOS wide-beam descending tracks of 476 and 124 (Figs 2g and h), covering regions on both sides of the fault rupture. (3) A portion of the ALOS wide-beam data from descending track 124 which we processed for this study (Fig. 2e), covering the footwall side of the fault. This portion of data is the same as that used by Fielding *et al*. (2013), with pre- and post-quake images taken 4 month before and a week after earthquake respectively. The ALOS wide-beam interferogram for track 124 is therefore split into two portions, with the hanging-wall processing result adopted from Fielding *et al*. (2013; Fig. 2g) and the footwall processing result taken from this study (Fig. 2e). This InSAR data set provides complete coverage of the surface rupture zone (Fig. 2).

The InSAR data were downsampled using a quadtree technique to reduce the number of data points by Shen *et al*. (2009) and Fielding *et al*. (2013). For the data from Shen *et al*. (2009), we assign 50 and 20 mm uncertainties for the ALOS and Envisat LOS changes, while ignoring spatial correlations between neighbouring pixels. Both uncertainties are higher than their nominal values by a factor

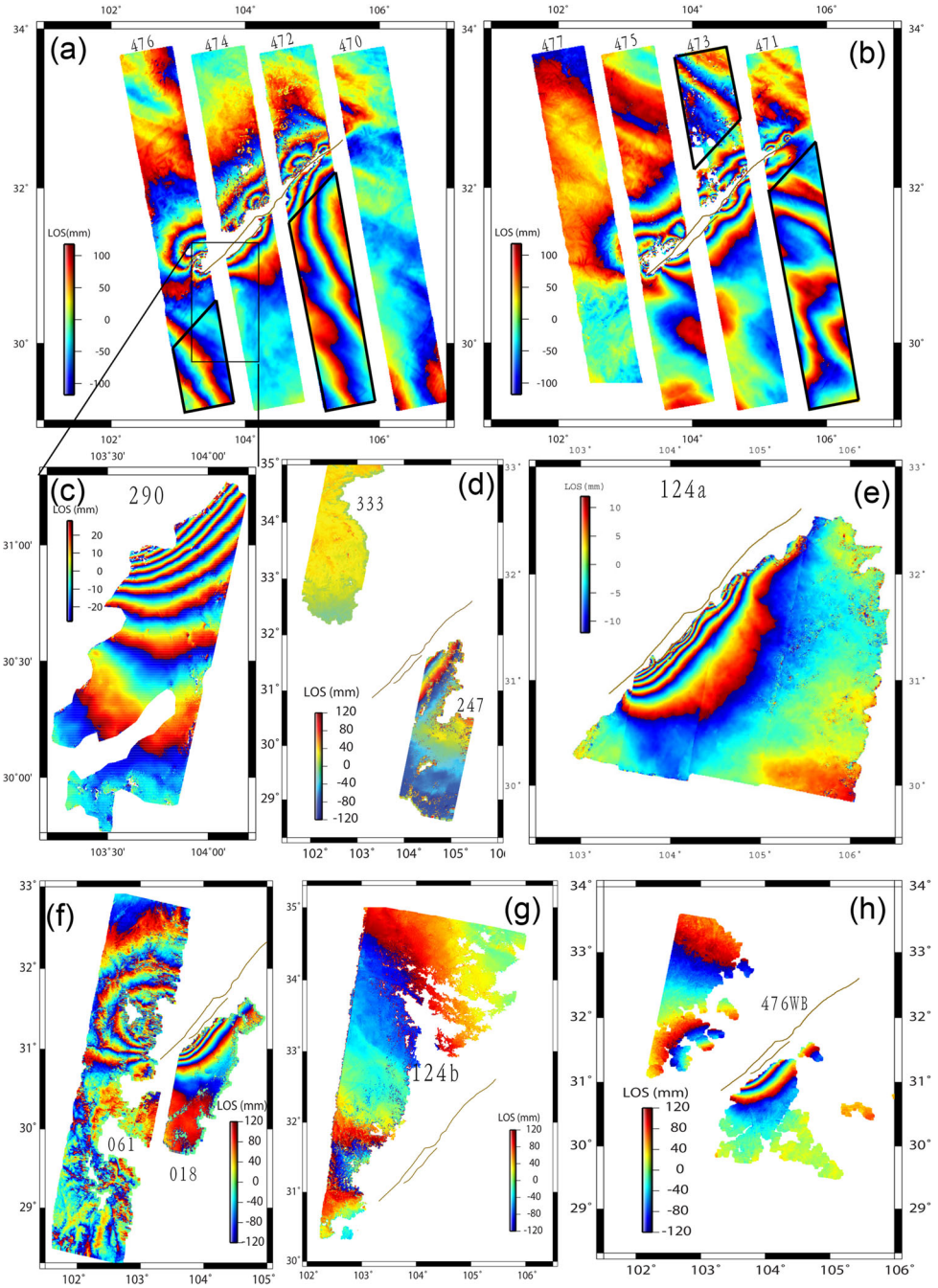

Figure 2. InSAR LOS interferograms used in this study. (a,b) ALOS data of tracks A470–A477 (interferograms rewrapped at 236 mm); (c) Envisat data of track D290 (interferograms rewrapped at 56 mm); (e) the foot-wall side of ALOS wide-beam data of track D124 (interferograms rewrapped at 23.6 mm); (d,f) Envisat data of tracks D333, D247, D061 and D018 (interferograms rewrapped at 240 mm); (g,h) ALOS wide-beam data of the hanging-wall side of tracks D124 and D476 (interferograms rewrapped at 240 mm). Parts of the data outlined with black frames in (a) and (b) are significantly affected by ionosphere disturbance and excluded from modelling.

of about two, to compensate for neglecting the spatial correlations of the InSAR data errors in data error propagation. Details about the data set can be found in Shen *et al*. (2009), and justification about the uncertainty assignment can be found in the supplement material #1. Uncertainties for both the ALOS and Envisat downsampled data from Fielding *et al*. (2013) are assigned to be 50 mm, as the data show greater noise level than our processed Envisat data, possibly due to unmodelled atmospheric disturbance. These uncertainties are assigned higher than their nominal uncertainties by a factor of about two or more, to compensate for neglecting the spatial correlations of the InSAR data errors in data error propagation. The downsampled data are shown in Supporting Information Fig. S1.

GPS coseismic displacement data are from two sources. One was from reoccupation of 158 stations of the Crustal Motion Observation Network of China project, and was produced by the Working Group of Crustal Motion Observation Network of China (2008). An updated version of the data set can be found in the supplemental material of Shen *et al*. (2009). Another data set was produced from reoccupation of a regional network of more than 300 stations maintained by the Sichuan Bureau of Surveying and Mapping of

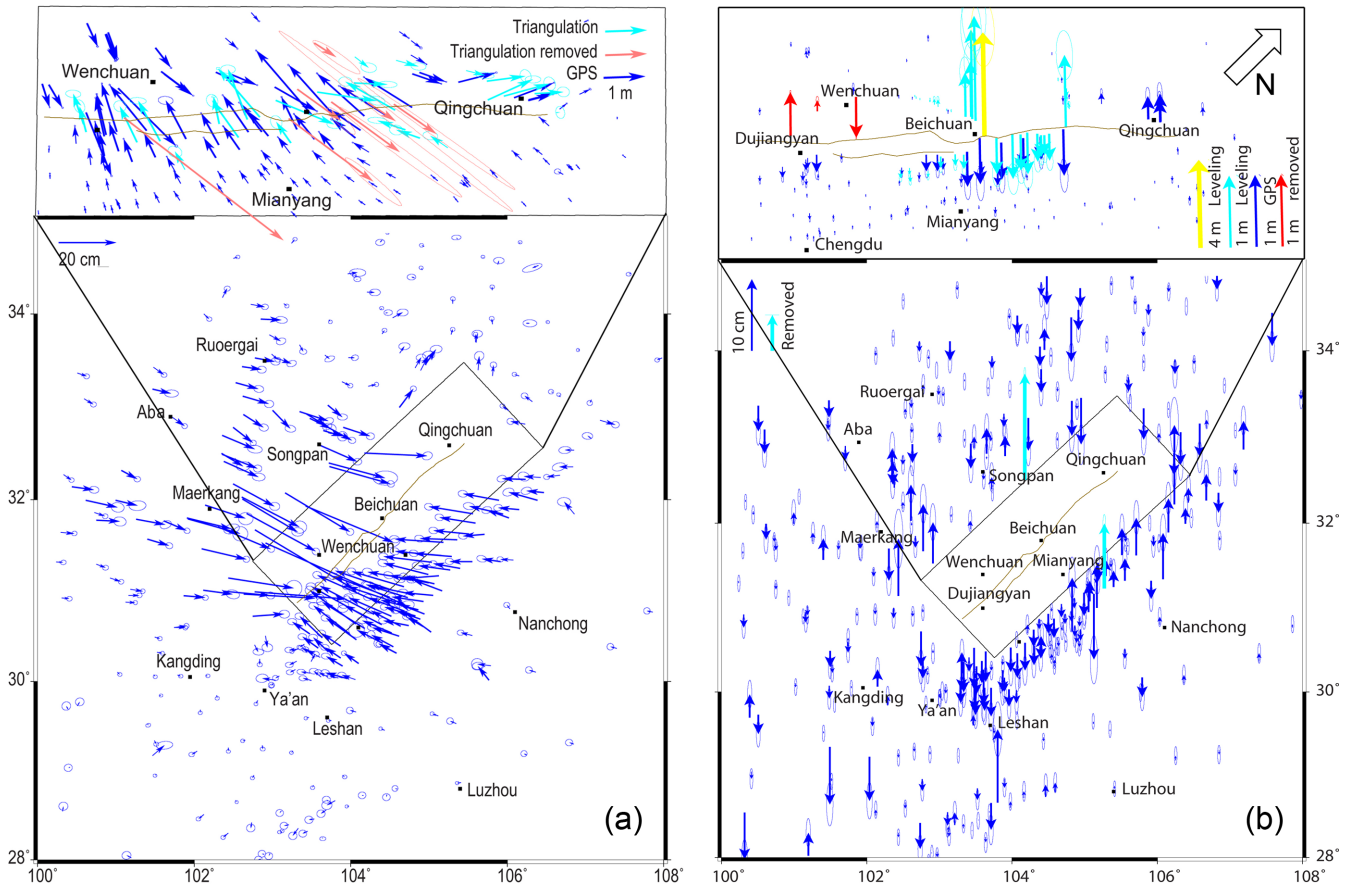

Figure 3. GPS, levelling, and triangulation data: (a) horizontal and (b) vertical. The enlarged map panels at the top of the figure are rotated clockwise by ~40°.

China and used by Wang *et al*. (2011). The combined GPS data set is shown in Fig. 3.

Coseismic levelling data were obtained from resurveying two second-order levelling routes in the hanging wall of the Longmen Shan fault. One of the routes runs across the fault rupture through Beichuan town (Wang *et al.* 2009; Fig. 3). The data set includes 42 measurements of vertical displacements relative to a far field reference site along the two survey routes, with the largest uplift recording of 4.711 m measured 0.5 km north of the surface rupture. The data were used by Wang *et al*. (2011) in their fault rupture model inversion and are adopted from their supplement material. Wang *et al*. (2011) also reoccupied a group of historical triangulation sites located close to the rupture using GPS, and derived 33 horizontal displacement vectors from the data set. These vectors are also adopted for this study.

Formal GPS data uncertainties provided by Wang *et al*. (2011) are usually at the millimetre or even sub-millimetre level, which are rather small for campaign GPS measurements. To account for more error sources usually associated with campaign GPS surveys such as antenna setup error, antenna phase centre error, and seasonal transient error, etc., we systematically increase the horizontal GPS data uncertainties by adding a factor of $D^{\frac{1}{4}}$ to the original formal errors, where D is the displacement amplitude in millimetre. Such a treatment enlarges uncertainties for all the sites, and assigns greater uncertainties for near-field sites which are more susceptive to non-elastic deformation caused by extreme strong ground motion, and also more affected by abrupt spatial variations of fault slip which may not be explained well by a smoothed fault slip model. The vertical GPS data and levelling data uncertainties are enlarged by 10 per cent of the data amplitudes from their original ones, to accommodate data errors which are much larger than those of the horizontal GPS data. Assignment of the 10 per cent enlargement of data error assigns larger errors for near-field sites for the same reasons given above, and is based on examination of overall post-fit residuals of the GPS vertical and levelling data.

In the modelling process data post-fit residuals are inspected, and 8 GPS vertical and 7 triangulation horizontal data in the near field are deemed to be outliers and removed from the modelling. We use 17 736 InSAR range change values, 424 GPS 3-component displacements, 42 levelling measurements, and 33 triangulation-GPS derived horizontal component data, weighted by their respective uncertainties described above, to invert for fault geometry and slip distribution (Supporting Information Figs S1 and S3 and Table S1).

3 COSEISMIC SLIP MODELLING

We assume that the Beichuan fault dips to the northwest and is listric in shape, based on geologic and seismic profile results of previous studies (Jia *et al.* 2006, 2010; Xu *et al.* 2009). The Pengguan fault is measured with a relatively shallower dip angle at the surface and is believed to root into the same decollement as the Beichuan fault at depth, but its exact geometry is not well determined. Aftershock locations are scattered (Huang *et al.* 2008; Zhu *et al.* 2008; Chen *et al.* 2009), and difficult to use for constraining fault geometry at depth, since they may result from distributed deformation off the fault (Tao *et al.* 2011). We therefore design a fault geometry model whose shape is directly constrained by the coseismic displacement data. The Xiaoyudong segment is omitted because of its

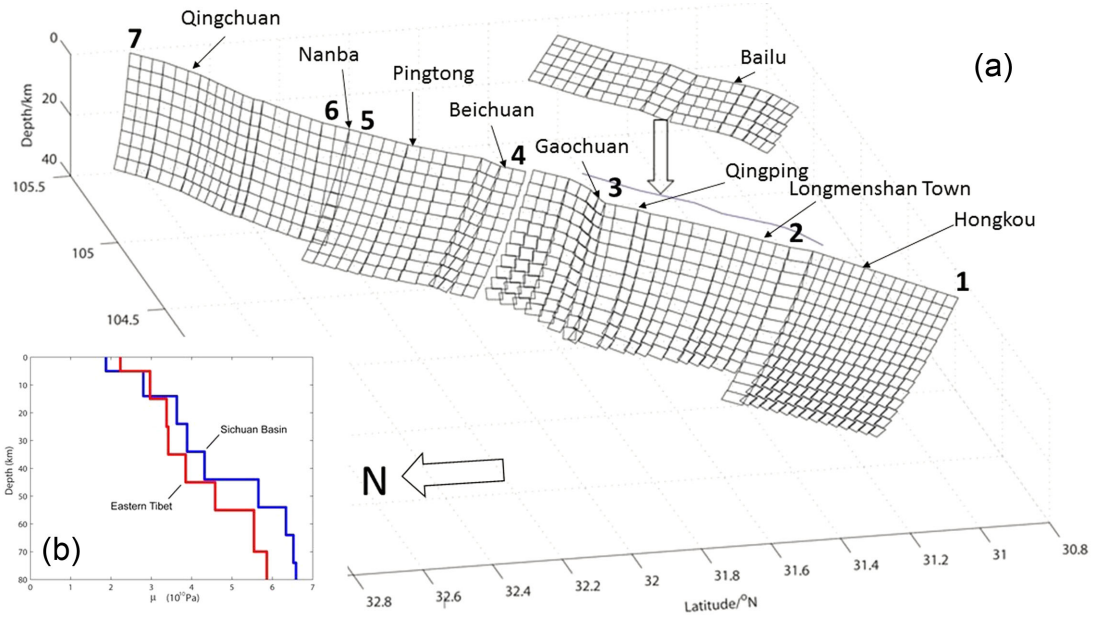

Figure 4. (a) Fault segment and optimized geometry model. The depth of the bottom edge of the model dislocation mesh varies from ~30 km in the SW to ~40 km in the NE. The numbers at top of the fault patches indicate locations of τ nodal points. (b) Shear modulus vertical profiles for Sichuan Basin and Eastern Tibet adopted from Huang *et al.* (2003).

small size and there is no near-field geodetic data to provide effective constraints on its slip distribution. The lateral extent of the model representations of the Beichuan and Pengguan fault ruptures are taken as 320 and 69 km long respectively. The Beichuan fault model is extended for about 80 km (50 km to the north and 30 km to the south, respectively) beyond the 240 km long surface rupture, following aligned aftershocks at both ends of the mapped Beichuan surface breaks.

Informed by geological constraints, we assume that the Beichuan fault is listric, and the fault downdip geometry follows the form of $z(x) = 2h_0/\pi$ arc tan (x/τ), where z is the depth of the fault plane, and x the horizontal distance of the fault plane from its surface trace. The fault plane is allowed to vary continuously along strike, with its downdip curvature dictated by the parameter τ. h_0 is the far-field fault plane depth to be solved for, and assumed to be the same for all the fault segments. That is, all faults are assumed to root into a regional detachment below the Tibetan Plateau (e.g. Li *et al.* 2010). τ is prescribed to vary linearly along strike within each segment between two nodal points, and the τ values are free parameters at several nodal points, to be solved for in the inversion. From northeast to southwest the Beichuan fault is divided into five segments, which are further meshed into 20 × 9, 14 × 11, 7 × 11, 13 × 11 and 15 × 14 patches, respectively. Each fault segment is sub-divided into rectangular patches roughly 4 × 4 km in size, and their geometries are determined by meshing the fault segments following the listric geometry described above and fitting each patch with a rectangular dislocation whose four edges are as close to the patch edges as possible. The Pengguan fault is assumed to have a single dip angle of 35° according to Jia *et al.* (2006, 2010), and the fault plane is divided into 20 × 5 rectangular patches roughly 4 × 4 km in size (Fig. 4). Slip on each patch is assumed uniform, and is inverted for together with the τ downdip curvature parameters, and a single value for h_0 in a nonlinear inversion procedure.

Geometry of the Beichuan fault near Nanba is believed to be complex, with aftershock data showing a right step at depth. We thus assign two independent τ values at this fault segment junction, allowing the fault plane to have a downdip offset across this junction point (Fig. 4). We therefore have 8 nonlinear parameters (i.e. seven τ values plus h_0) in our model and 1728 parameters of strike- and dip-slip components on 864 fault patches. We also have 16 scenes of InSAR data, which add additional parameters to estimate (Fig. 2). For ALOS paths 472, 473, 474, and the wide-beam 476, the interferograms are broken into two pieces by data gaps across the fault, and two offset parameters are needed for the southern and northern pieces of each interferogram, respectively. For the other six scenes, one offset parameter is needed for each of them. The total number of free interferogram parameters is 20 for all of the InSAR images. The total number of parameters in the model is 1756.

As revealed by seismic profile and tomographic studies, the crustal structure across the Longmen Shan range is rather complex, and the strong contrast in crustal structure across the Longmen Shan affects the elastic deformation field associated with the coseismic rupture (Huang *et al.* 2003; Wang *et al.* 2007; Yao *et al.* 2008; Liu *et al.* 2009; Zhang *et al.* 2009b; Xu & Song 2010). To the southeast, the Sichuan Basin has a soft sediment layer with relatively low seismic velocities in the upper crust, but strong lower crust and upper mantle with higher seismic velocities. To the northwest, on the other hand, the Songpan-Ganzi block has a strong upper crust composed of Mesozoic rocks and with Precambrian rocks outcropping on the hanging wall side of and close to the fault (Burchfiel *et al.* 1995, 2008). Its lower crust, in contrast, has an extensive low seismic velocity zone interpreted as a zone rich in melt and/or crustal fluids (Liu *et al.* 2009). The significant lateral contrast of crustal structure across the Longmen Shan range inevitably affects the deformation field, and therefore should be accounted for in the model. In our modelling we consider several elastic 1-D structures on either side of the Longmen Shan derived from previous studies: (a) a regional tomography model of Huang *et al.* (2003), (b) a regional tomography model of Wang *et al.* (2007), and (c) a regional receiver function study of Liu *et al.* (2009). These three models share similar features despite some differences in detail, and the results from using the three models are similar. We adopt the crustal

Table 1. Earth structure model adopted from Huang *et al*. (2003).

No	Sichuan Basin				Eastern Tibet			
	Depth	Density (kg^{-1} m^{-3})	Shear modulus (10^{10} Pa)	Young's Modulus (10^{10} Pa)	Depth	Density (kg^{-1} m^{-3})	Shear Modulus (10^{10} Pa)	Young's Modulus (10^{10} Pa)
1	0.0–5.0	2452.0	1.87	4.68	0.0–5.0	2528.0	2.23	5.58
2	5.0–14.0	2630.0	2.80	7.00	5.0–15.0	2657.0	2.97	7.42
3	14.0–24.0	2778.0	3.63	9.08	15.0–25.0	2728.0	3.38	8.44
4	24.0–34.0	2826.0	3.89	9.71	25.0–35.0	2736.0	3.42	8.54
5	34.0–44.0	2898.0	4.32	10.80	35.0–45.0	2820.0	3.85	9.63
6	44.0–54.0	3105.0	5.65	14.13	45.0–55.0	2938.0	4.58	11.45
7	54.0–64.0	3208.0	6.34	15.85	55.0–70.0	3088.0	5.54	13.86
8	64.0–74.0	3260.0	6.52	16.43	70.0–80.0	3161.0	5.86	14.77
9	74.0–80.0	3269.0	6.58	16.59	80.0–∞	3161.0	5.86	14.77
10	80.0–∞	3269.0	6.58	16.59				

structure model of Huang *et al*. (2003), since data fitting to this model is slightly better than the other two (details to be presented in Section 5), and its structural parameters for the Songpan-Ganzi block and Sichuan basin are listed in Table 1. In addition to the three regional structure models we also test a model assuming a homogeneous half-space for the Earth structure for comparison, and find significant improvement of data fitting using Huang *et al*.'s model over the homogeneous half-space model. We therefore adopt the crustal structure model from Huang *et al*. (2003) in our inversion and final result presentation.

We start the model assuming a uniform dip angle of 50° for all of the Beichuan fault segments, and use a Newtonian nonlinear inversion procedure to solve for the coseismic slip distribution. The problem is defined as:

$$\mathbf{y} = \mathbf{A}\mathbf{x} + \mathbf{e} \tag{1}$$

where $\mathbf{y}$ is an $n\times1$ array composed of the geodetic data and n is the total number of data points. The GPS data are the east, north, and up components of coseismic displacements (Fig. 3), the InSAR data are the downsampled coseismic line-of-sight changes with respect to a far-field reference pixel in each image (Fig. 2 and Supporting Information Fig. S1), the levelling data are coseismic elevation changes with respect to a distant reference site (inset close-up, Fig. 3b), and the triangulation data are adjusted station east and north displacements (Fig. 3a), respectively. The model vector $\mathbf{x}$ is an array of $m_1\times1$, composed of two parts; the first part involves the strike and dip components of coseismic slip on fault patches, and the second part has the 20 InSAR interferogram offsets (including the across-fault offsets for paths 472, 473, 474, and wide-beam 476). The model kernel $\mathbf{A}$ is an $n \times m_1$ array, linking the unknowns of fault slip and the interferogram constants linearly to the observations. $\mathbf{A} = \mathbf{A}(\mathbf{z})$, where $\mathbf{z} = (\tau_1, \tau_2, \ldots \tau_7, h_0)$ are the nonlinear parameters of fault curvature and depth to detachment. $\mathbf{e}$ is an $n\times1$ array for data errors. $\mathbf{e} \sim \mathrm{N}(0, \mathbf{C}_\mathrm{d})$, where $\mathbf{C}_\mathrm{d}$ is the variance/covariance matrix of the errors.

We impose a first-order smoothing constraint to the fault slip components, in the form of

$$\mathbf{0} = \mathbf{G}\mathbf{x} + \mathbf{h}, \tag{2}$$

where $\mathbf{G}$ is a $p\times m_1$ array for imposing p constraints to the solution. For each pair of adjacent fault patches (in both along-strike and updip directions), the entries are 1 and -1 for the corresponding pair of slip components, and 0 for the rest of the components. $\mathbf{h}$ is a $p\times1$ array of *a priori* errors. $\mathbf{h} = \mathrm{N}(0, \mathbf{C}_\mathrm{a})$, where $\mathbf{C}_\mathrm{a}$ is the variance/covariance matrix of the *a priori* errors, composed of non-zero diagonal terms only. A uniform smoothing is assigned for all the neighbouring pairs. We also impose positivity constraints to the solution; that is, left-lateral and normal slips are not allowed. The positivity constraints are applied iteratively in each round of solution, with the largest 'negative' slip being constrained to zero in each step. The iteration continues till no more 'negative' slip on fault patches exists.

The joint equations for data and *a priori* constraints are:

$$\begin{bmatrix}\mathbf{y}\\ \mathbf{0}\end{bmatrix} = \begin{bmatrix}\mathbf{A}\\ \mathbf{G}\end{bmatrix}\mathbf{x} + \begin{bmatrix}\mathbf{e}\\ \mathbf{h}\end{bmatrix} \tag{3}$$

In the first step we assume a set of nonlinear parameters $\mathbf{z}_0$. Let $\mathbf{y} = \mathbf{A}(\mathbf{z}_0)\,\mathbf{x} + \mathbf{e}$, a least squares solution yields:

$$\mathbf{x}_0 = \left(\mathbf{A}^\mathrm{T}\mathbf{C}_\mathrm{d}^{-1}\mathbf{A} + \mathbf{G}^\mathrm{T}\mathbf{C}_\mathrm{a}^{-1}\mathbf{G}\right)^{-1}\mathbf{A}^\mathrm{T}\mathbf{C}_\mathrm{d}^{-1}\mathbf{y} \tag{4}$$

The first round post-fit residuals are:

$$\begin{bmatrix}\mathbf{dy}_1\\ \mathbf{db}_1\end{bmatrix} = \begin{bmatrix}\mathbf{y}\\ \mathbf{0}\end{bmatrix} - \begin{bmatrix}\mathbf{A}(\mathbf{z}_0)\\ \mathbf{G}\end{bmatrix}\mathbf{x}_0 \tag{5}$$

Taking the first-order perturbation of the observables:

$$\mathbf{dy} = \mathbf{A}\mathbf{dx} + \frac{\partial\mathbf{A}}{\partial\mathbf{z}}\mathbf{x}\mathbf{dz} + \mathbf{e} \tag{6}$$

Or, $\mathbf{dy} = [\,\mathbf{A}\;\mathbf{B}\,]\left[\begin{smallmatrix}\mathbf{dx}\\ \mathbf{dz}\end{smallmatrix}\right]$, where $\mathbf{B} = \frac{\partial\mathbf{A}}{\partial\mathbf{z}}\mathbf{x}$, which are the numerically derived partial derivatives with respect to the fault curvature parameters.

Let the post-fit residuals link to the parameter increments:

$$\begin{bmatrix}\mathbf{dy_1}\\ \mathbf{db_1}\end{bmatrix} = \begin{bmatrix}\mathbf{A}(\mathbf{z_0}) & \mathbf{B}(\mathbf{z_0},\mathbf{x_0})\\ \mathbf{G} & \mathbf{0}\end{bmatrix}\begin{bmatrix}\mathbf{dx}\\ \mathbf{dz}\end{bmatrix} + \begin{bmatrix}\mathbf{e}\\ \mathbf{h}\end{bmatrix} \tag{7}$$

Solve above equations by least squares to obtain $\mathbf{dx}_1$ and $\mathbf{dz}_1$:

$$\begin{aligned}\begin{bmatrix}\mathbf{dx}_1\\ \mathbf{dz}_1\end{bmatrix} = &\left[\begin{pmatrix}\mathbf{A}^\mathrm{T}\\ \mathbf{B}^\mathrm{T}\end{pmatrix}\mathbf{C}_\mathrm{d}^{-1}\begin{pmatrix}\mathbf{A} & \mathbf{B}\end{pmatrix} + \begin{pmatrix}\mathbf{G}^\mathrm{T}\\ \mathbf{0}\end{pmatrix}\mathbf{C}_\mathrm{a}^{-1}\begin{pmatrix}\mathbf{G} & \mathbf{0}\end{pmatrix}\right]^{-1}\\ &\times\left[\begin{pmatrix}\mathbf{A}^\mathrm{T}\\ \mathbf{B}^\mathrm{T}\end{pmatrix}\mathbf{C}_\mathrm{d}^{-1}\mathbf{dy}_1 + \begin{pmatrix}\mathbf{G}^\mathrm{T}\\ \mathbf{0}\end{pmatrix}\mathbf{C}_\mathrm{a}^{-1}\mathbf{db}_1\right]\end{aligned} \tag{8}$$

Let $\mathbf{z}_1 = \mathbf{z}_0 + \mathbf{dz}_1$, $\mathbf{x}_1 = \mathbf{x}_0 + \mathbf{dx}_1$, the second round post-fit residuals are:

$$\begin{bmatrix}\mathbf{dy}_2\\ \mathbf{db}_2\end{bmatrix} = \begin{bmatrix}\mathbf{y}\\ \mathbf{0}\end{bmatrix} - \begin{bmatrix}\mathbf{A}(\mathbf{z}_1)\\ \mathbf{G}\end{bmatrix}\mathbf{x}_1 \tag{9}$$

Then we solve

$$\begin{bmatrix}\mathbf{dy}_2\\ \mathbf{db}_2\end{bmatrix} = \begin{bmatrix}\mathbf{A}(\mathbf{z}_1) & \mathbf{B}(\mathbf{z}_1)\\ \mathbf{G} & \mathbf{0}\end{bmatrix}\begin{bmatrix}\mathbf{dx}_2\\ \mathbf{dz}_2\end{bmatrix} + \begin{bmatrix}\mathbf{e}\\ \mathbf{h}\end{bmatrix} \tag{10}$$

by least squares to obtain $\mathbf{dx}_2$ and $\mathbf{dz}_2$.

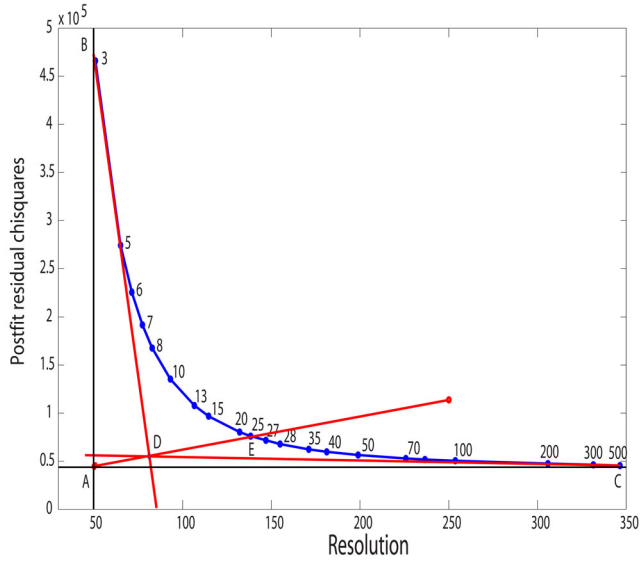

Figure 5. Trade-off between data post-fit residual chi-squares χ_d^2 and resolution R. The number labels in the figure are the uncertainties of the smoothing constraints (in centimetre) imposed on fault slip of neighbouring patches.

Continue the iteration until the weighted post-fit χ^2 reduction becomes negligible (<0.1). The post-fit χ^2 is defined as:

$$\chi^2 = \mathbf{dy}^{\mathrm{T}}\mathbf{C}_{\mathbf{d}}^{-1}\mathbf{dy} + \mathbf{db}^{\mathrm{T}}\mathbf{C}_{a}^{-1}\mathbf{db} \tag{11}$$

The resolution matrix is (Jackson & Matsu'ura 1985):

$$R = \left(\mathbf{A}^{\mathrm{T}}\mathbf{C}_{\mathbf{d}}^{-1}\mathbf{A} + \mathbf{G}^{\mathrm{T}}\mathbf{C}_{\mathbf{a}}^{-1}\mathbf{G}\right)^{-1}\mathbf{A}^{\mathrm{T}}\mathbf{C}_{\mathbf{d}}^{-1}\mathbf{A} \tag{12}$$

which takes into account all the variance of the data and *a priori* constraints and incorporates all the variance/covariance of the solution. The sum of the diagonal terms of **R** is the total number of resolution (i.e. the rank of the resolution matrix) resolved by the data (Jackson & Matsu'ura 1985). The post-fit residual χ_d^2 due to observational data is defined as $\chi_d^2 = \mathbf{dy}^{\mathrm{T}}\mathbf{C}_{\mathbf{d}}^{-1}\mathbf{dy}$, and the reduced post-fit residual χ_r^2 due to data is:

$$\chi_r^2 = \frac{\mathbf{dy}^{\mathrm{T}}\mathbf{C}_{\mathbf{d}}^{-1}\mathbf{dy}}{n - \sum[\mathrm{digonal}\,(R)]} \tag{13}$$

where n is the total number of data.

Slip on individual fault patches is linked to the geodetic measurements at the Earth's surface using the PSGRN/PSCMP software (Wang *et al.* 2006) to compute dislocation-induced surface displacements in a layered media. The partial derivatives for the nonlinear parameters are derived numerically. When computing the Green's functions, we treat the regions northwest and southeast of the Beichuan fault differently, adopting the 1-D elastic structure (Table 1) of the Songpan-Ganzi block for stations on the northwest side and the Sichuan Basin structure for stations on the southeast side for the Green's function evaluation.

One of the challenging issues in dealing with a geophysical inverse problem is the proper assignment of *a priori* constraints to the solution; and in our case, it is about the degree of smoothing to the slip distribution. We test a wide range of *a priori* smoothing constraints (i.e. uncertainty for error **h**, equation 10), ranging from 3 to 500 cm. The results are plotted in Fig. 5, which shows the trade-off between data post-fit residual chi-squares χ_d^2 and the resolution (see Shen *et al.* [1996] for resolution interpretation). There are multiple ways to select the optimal solution based on various considerations, and here we choose an approach that we consider robust and reasonable, and is close to the maximum curvature in a Tikhonov plot (Hearn & Bürgmann 2005). The vertical line AB in Fig. 5 marks the minimum resolution when the solution is constrained to the extreme, and the horizontal line AC marks the minimum post-fit residual when the solution is free of constraints. The line BD is the asymptote extrapolated from the three largest post-fit residual chi-square points, and the line CD is the asymptote extrapolated from three smallest post-fit residual chi-square points, respectively. The line AD crosses the trade-off curve at point E, which denotes the solution with the preferred constraints for the inversion. In this case we determine that the chosen model corresponds to a 250 mm uncertainty for the *a priori* smoothing constraints. The slip resolutions for the optimal fault geometry are shown in Fig. 6. It shows very high resolution for shallow slip, suggesting that the results of peak slips near the surface are quite robust. The resolution is relatively low near the bottom of the fault rupture, suggesting that slip on individual fault patches there may not be well resolved and reliable. Average slip over a panel of several patches, however, has much better resolution and reliability. Among all of the 1828 slip parameters only 138 degrees of freedom are resolved by real data (Fig. 5), and the rest are constrained by the *a priori* smoothing constraints.

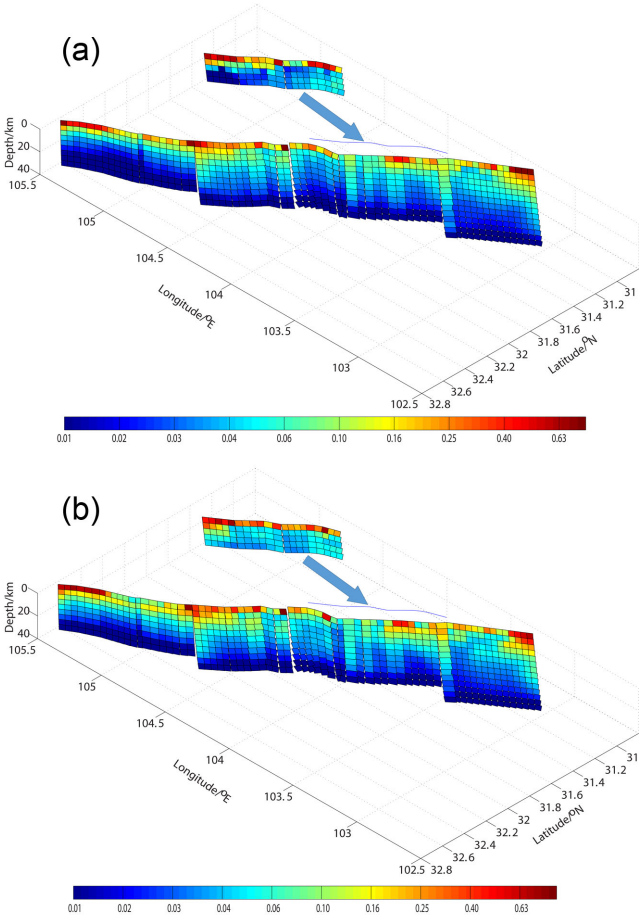

Figure 6. Slip resolution distribution on fault planes. (a) Strike-slip component; (b) dip-slip component.

We also test the impact of different weighting between the GPS and InSAR data to the solution. We run a range of solutions with weighting of the InSAR data relative to GPS increased by up to 50 per cent or reduced by 33 per cent. The results show some minor changes, but the overall pattern such as the basic fault geometry and locations of the high slip concentrations are unchanged.

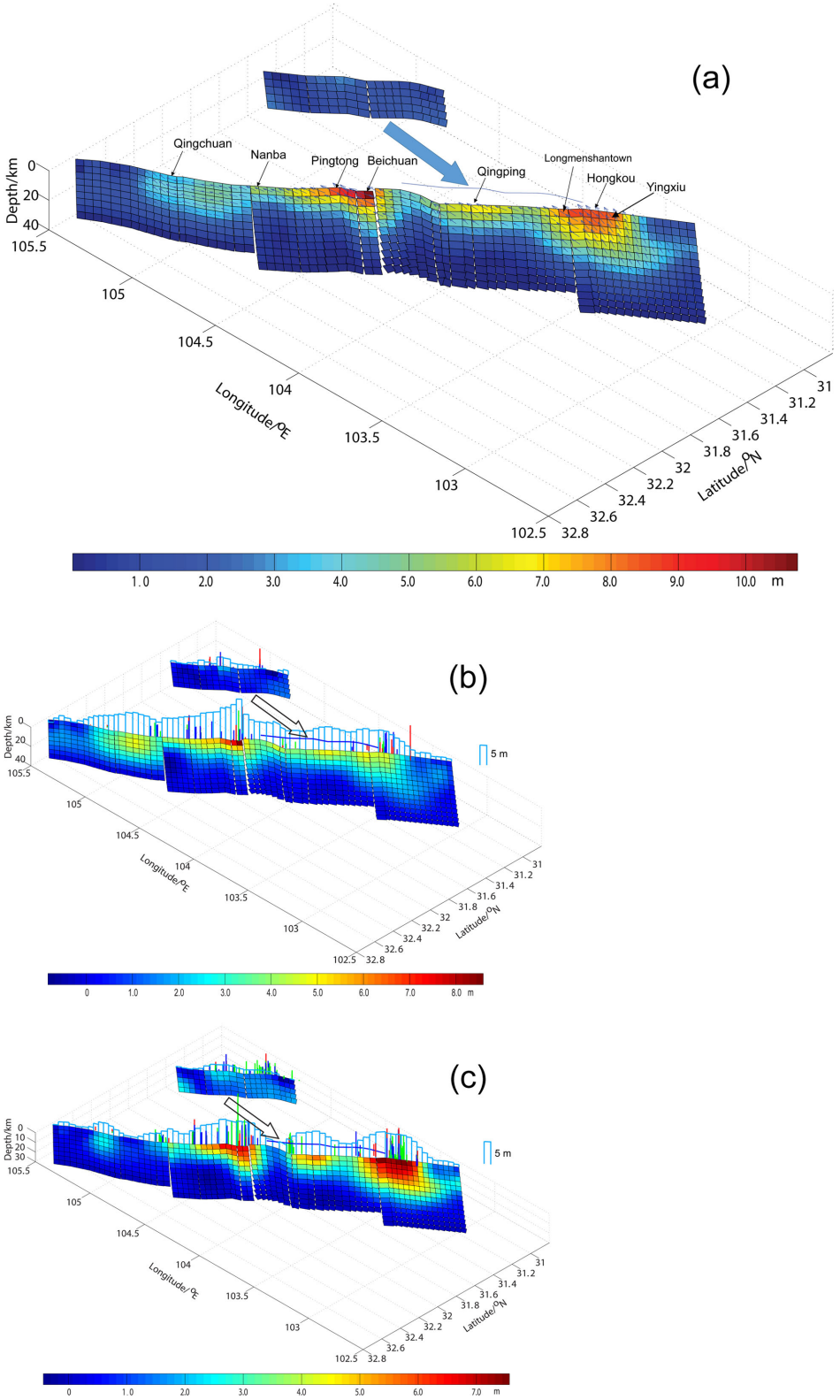

Figure 7. Fault slip model. (a) Vectors and colours of patches denote slip rake angles and amplitudes. (b) Right-lateral strike-slip component. (c) Thrust-slip component. Vertical bars on top of the fault patches are observed surface offsets, blue by Xu *et al.* (2009), green by Liu-Zeng *et al.* (2009) and red by Lin *et al.* (2009), respectively. The light blue bars at the same places are model-predicted surface offsets.

4 RESULTS

The preferred fault slip model is presented in Fig. 7 and listed in Supporting Information Table S1. The GPS, triangulation, and levelling data fitting results are in Supporting Information Tables S2 and S3. For the fault geometry resolved in our model, we find that fault dip angles vary gradually from southwest to northeast. The Beichuan fault dips at 36° near the surface at its southwest end and is close to vertical (83°) at its northeast end at the surface (Fig. 4a). The fault-plane dips decrease with increasing depth for the southwest segment, and the dip angle at the bottom of the rupture shallows to ∼26° at 20 km depth. As the dip angle gets shallower downdip the data provide weaker constraints on the fault depth, the result becomes less certain for fault geometry below 10 km depth. The shallow Beichuan fault dips 43°, 67°, and 51° at Hongkou, Qingping, and Beichuan (Fig. 4a). It is segmented near Nanba, with the surface fault dip angle jumping from ∼51° to ∼70° from southwest to northeast (Fig. 4a). Such a geometric discontinuity appears to be consistent with the aftershock distribution, with the deeper aftershocks along the two segments appearing to be systematically offset by about 5 km (Chen *et al.* 2009). The Pengguan fault dips at 35° and reaches 11 km depth where it merges into the Beichuan fault.

Our optimal model is able to achieve 96.4 per cent reduction of the observation data variance after model fitting, and the reduced post-fit residual RMS $\sqrt{\chi_r^2}$ is 1.936. The model predicted LOS changes for InSAR measurements are shown in Fig. 8, and fit to the InSAR data is plotted in Fig. 9. The result shows that although some parts of the data may not be well explained, the overall fit to the model is quite reasonable. Compared to our previous solution (Shen *et al.* 2009), the fit to the data has been improved, particularly for near-field InSAR measurements. Negative range-change residuals of SAR interferograms south of the Beichuan fault in our previous solution disappear in our current solution, indicating that the listric fault geometry model indeed improved data fitting, and the surface displacement data agree better with a model that has a relatively steep fault plane at shallow depth and a gently dipping fault plane at greater depth. Compared to the data fitting of Fielding *et al.* (2013), our result shows significant residual reduction for the ALOS interferogram of wide-beam track 124 on the foot-wall side, a slight increase of the residuals for Envisat track 018, and about the same level for the rest of the interferograms.

Some large residuals of the InSAR data in the intermediate and far field range from the fault are produced by ionospheric disturbances and cannot be modelled. This includes the southern parts of tracks 471, 472 and 476, and the northern part of track 473, which we excluded from the model inversion (Fig. 2). This finding is consistent with previous studies (Hao *et al.* 2009; Hashimoto *et al.* 2009; Shen *et al.* 2009; Feng *et al.* 2010; Tong *et al.* 2010; Wang *et al.* 2011; Fielding *et al.* 2013).

The model fits most of the near and intermediate field GPS vectors well, with about 90 per cent of the near-field sites fit within their 95 per cent of confidence regions (Fig. 10). The model underestimates the far-field displacements by several centimetres in the hanging wall, possibly due to post-seismic displacements included in the observations that are not accounted for in the model (GPS post-seismic surveys of the sites were made a few months to more than a year after the quake [Wang *et al.* 2011]). Such systematic residuals are likely due to slip on the downdip extension of the listric fault extended to the far field, as modelled by Wang *et al.* (2011). While the quantification of post-seismic deformation is beyond the scope of this study, near field GPS post-seismic observations did demonstrate several centimetres of displacements at the hanging wall sites a few months after the quake (see e.g. fig. S1 in Supplement Material of Shen *et al.* 2009). The GPS vertical data are quite scattered and suffer from large uncertainties, which is not surprising because the pre-earthquake measurements were made with only a few hours of occupation and with antennas set up on tripods (Wang *et al.* 2011). These data do not provide much constraint to the solution. The largest vertical displacements in the levelling data occurred on near-field sites within a couple of kilometres from the fault, and are therefore sensitive to unmodelled complexity of shallow fault structure and slip variations. As described above, these data have been downweighted by adding 10 per cent of the amplitudes of measurements to their uncertainties. The coseismic displacement vectors derived from GPS/triangulation near field observations, are useful in resolving finer slip detail despite of their larger misfits and larger data uncertainties.

The slip distribution resolved in our model includes five slip peak zones near the surface (Fig. 7). The largest peak slip is along the southwest segment from Yingxiu to Longmen Shan Town, with two peaks near Longmen Shan Town and Hongkou respectively (Table 2). It also extends downdip, with ∼5 m thrust at 10–15 km depth, in the vicinity of the earthquake epicentre. The second largest peak slip is near Beichuan, extending for almost 50 km from Beichuan to Pingtong. The third, fourth, and fifth largest peak slips are near Qingping, Qingchuan, and Nanba, respectively (Table 2). The Qingping and Qingchuan peak slips are more smoothly distributed than the other ones, and the dextral slip in the Qingchuan segment reached deeper than along most of the other segments, with ∼3 m slip at ∼15 km depth. The high slip concentration at Nanba is on the southwest side of the fault junction only, suggesting that the stepping geometry of the fault at depth impeded the rupture to propagate across the junction. Slip on the Pengguan fault is dominated by thrust faulting, with 1–2 m of slip over most parts of the fault plane. The highest thrust motion of ∼2.4 m is found at the northern end of the Pengguan fault at ∼6–9 km depth, although the resolution is low there.

We evaluated six elastic structure models, three of which (Huang *et al.* 2003; Wang *et al.* 2007; Liu *et al.* 2009) have separate layered structures on both sides of the Beichuan fault, two have a uniform layered structure with either a representative Sichuan Basin or Eastern Tibet structure (Huang *et al.* 2003; Fig. 4b), and one is a homogeneous elastic half-space. Comparing the shear modulus of the three layered models, on the Sichuan Basin side the three models are about the same in the depth range of 15–40 km. In the shallow (0–15 km) and deep (40–80 km) depth ranges, the values of Liu *et al*. and Wang *et al*. are notably lower and greater than that of Huang *et al.* respectively (Supporting Information Fig. S2a). At the Eastern Tibet side, the three models are about the same except that in the depth range of 40–80 km the values of Wang *et al*. are significantly smaller than that of the other two models (Supporting Information Fig. S2a). Comparisons of Young's modulus of the three models are similar to the shear modulus comparisons (Supporting Information Fig. S2b). During each of the model inversions the best fitting fault geometry is sought. The results yield the weighted data post-fit residual RMS of 1.936, 2.018, and 1.942 for using the structure models of Huang *et al.* Wang *et al.* and Liu *et al.* respectively, with the one using Huang *et al*.'s model slightly smaller than the other two. The post-fit residual RMS for using the homogeneous half-space model is 2.059. The F-test results show that better data fitting is achieved using Huang *et al*.'s model compared to using Liu *et al*.'s model (at the 66 per cent confidence), Wang *et al*.'s model (at the 99 per cent confidence), and the homogeneous half-space model

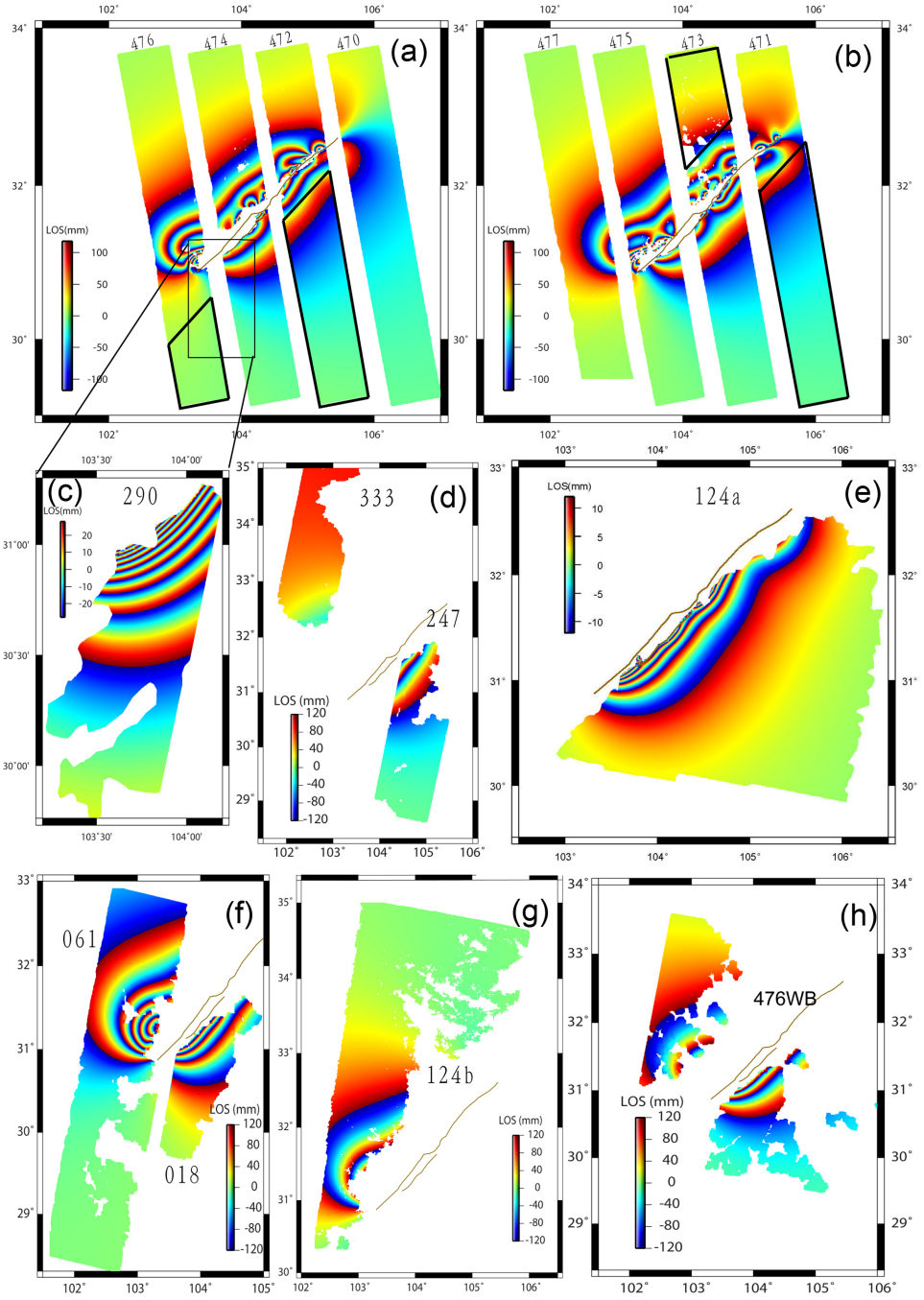

Figure 8. Model-predicted LOS changes for InSAR measurements. Original data are shown in Fig. 2, and the interferograms are rewrapped the same way as in Fig. 2. Parts of the data outlined with black frames are significantly affected by ionosphere disturbance and excluded from modelling.

(at the 99 per cent confidence) (for details of the F-test algorithm see Shen *et al.* 1996).

We also test two other layered structure models, one assuming the Sichuan Basin and the other the Songpan-Ganzi structure of Huang *et al.*'s model for the entire region, and run for solution through the nonlinear least-squares procedure. The reduced post-fit residual chi-squares are 1.970 and 1.949 for the Sichuan Basin and Songpan-Ganzi structure models respectively, indicating that both models fit the GPS and InSAR data worse than the one using the complete Huang *et al.*'s structure model at the 99 per cent and 82 per cent of confidence, respectively. This result confirms that inclusion of lateral change of crustal structure in model setting improved the modelling.

According to our model, the total seismic moment released during the Wenchuan earthquake is 1.23×10^{21} N m (assuming a constant shear modulus of 3×10^{10} Pa), which is equivalent to a M_w 8.06 event. However, if we take only the slip above 20 km depth; that is, ignoring the slip below 20 km depth, which is likely dominated by afterslip, the seismic moment release becomes 8.2×10^{20} N m, equivalent to an M_w7.9 event. The latter estimate is close to the co-seismic moment release estimated from global teleseismic data and consistent with most of the previous estimates using seismological

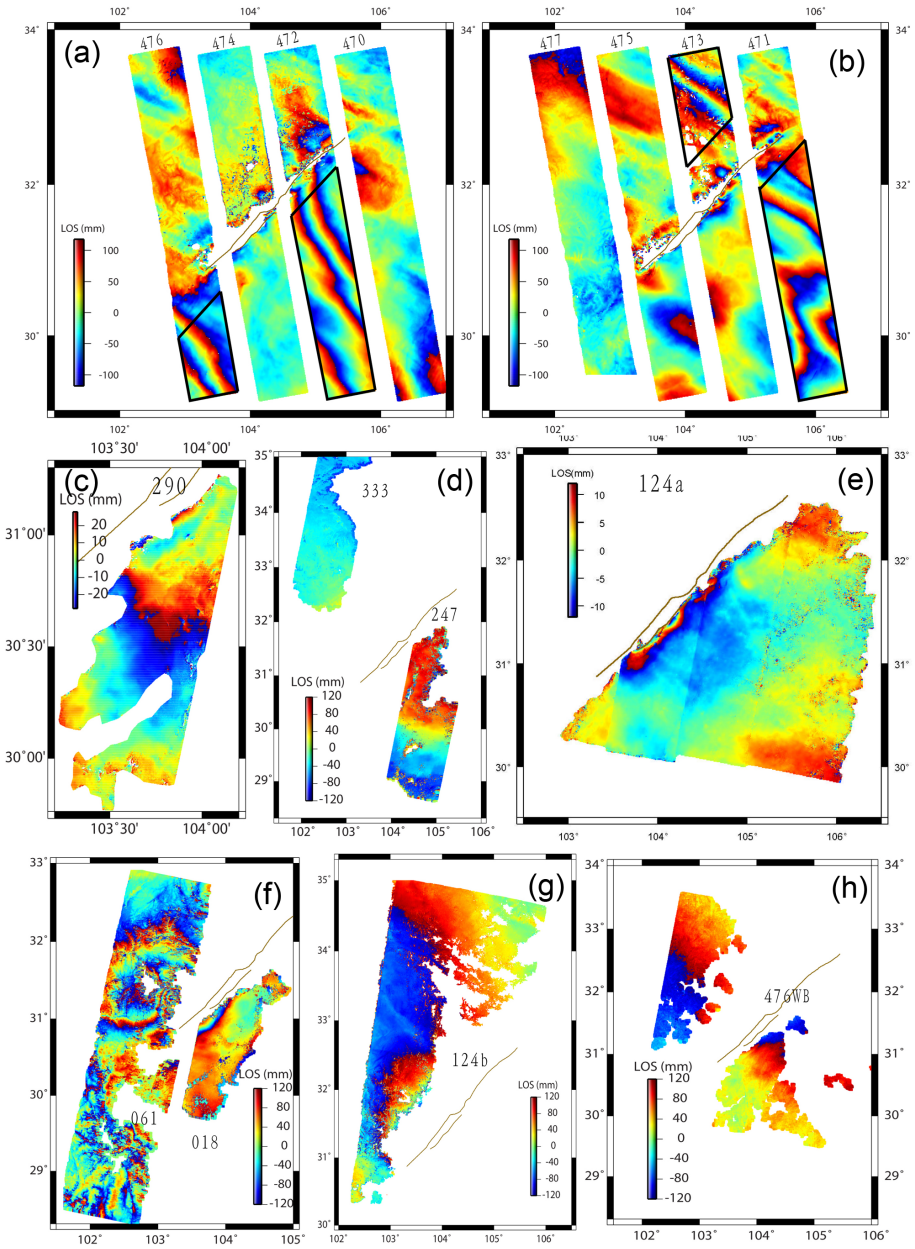

Figure 9. InSAR LOS data post-fit residuals. The data are shown in Fig. 2, and the interferograms are rewrapped the same way as in Fig. 2. Parts of the data embraced with black frames are significantly affected by ionosphere disturbance and excluded from modelling.

and/or geodetic data (e.g. Wang *et al.* 2008; Zhang *et al.* 2009a; Hao *et al.* 2009; Tong *et al.* 2010; Wang *et al.* 2011). The seismic moments released on the local slip concentrations are equivalent to events of M_w7.5 near Yingxiu/Hongkou, M_w7.3 near Beichuan, M_w7.2 near Qingping, M_w7.1 near Pingtong, and M_w6.7 near Nanba, respectively (Table 2).

5 DISCUSSION

5.1 Comparison of results with fault surface offset observations

The inverted slip distribution at the surface agrees well with surface offsets measured in the field. For the dip-slip component, the inverted slip distribution at the surface agrees remarkably well with measured vertical offsets at Hongkou, Longmen Shan Town, Qingping, Beichuan, Pingtong, and Nanba (Fig. 7c). The only two exceptions are: (a) our estimated vertical offset of ~6.5 m at Beichuan disagrees with a measurement of 10.8 m made by Liu-Zeng *et al.* (2009). The latter estimate, however, seems to be an outlier and is twice as much as other field measurements in the area; and (b) our inverted vertical offsets of ~1 m or less along the Pengguan fault are in general smaller than field observations, which are usually ≥1 m, and as large as 3–4 m in places. Most of the disagreements between our results and geologically measured surface offsets along the Pengguan fault are probably due to: (a) spatial smoothing of our model, as the geologically measured offsets show significant fluctuations along strike; (b) the uniform dip geometry adopted in our model, which may differ significantly from a steeper geometry at shallow depths at some places, resulting in under predicting the vertical offsets at the surface; (c) slip overshoot at shallow depth; and

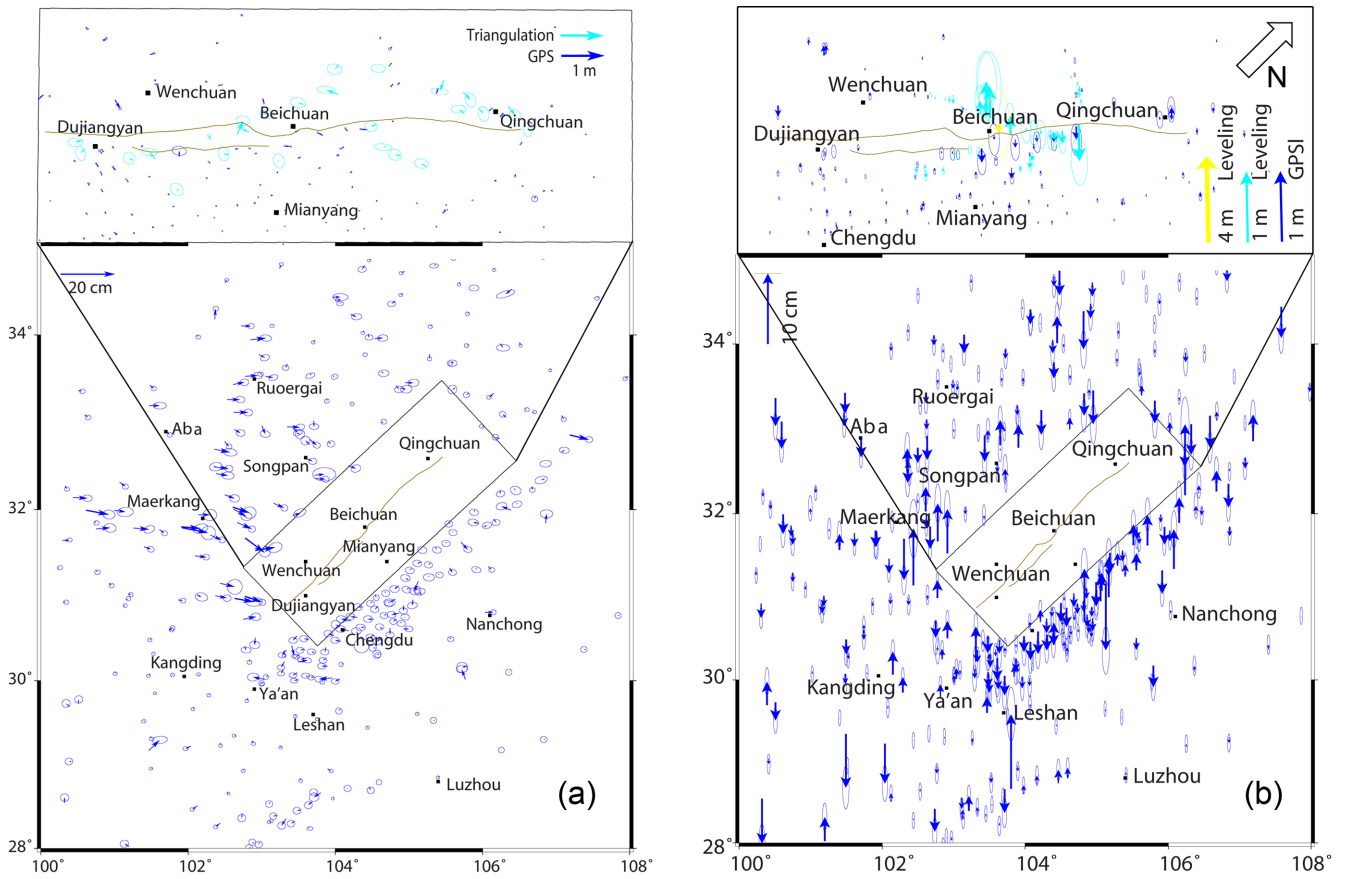

Figure 10. Post-fit residuals of GPS, triangulation and levelling data. (a) Horizontal and (b) vertical components. The enlarged map panels at the top of the figure are rotated clockwise by ~40°.

Table 2. Peak slip statistics.

Peak slip zone	Strike (m)	Thrust (m)	Seismic moment (N m)	Equivalent magnitude (M_w)
Yingxiu-LMST (Yingxiu)	4.0	7.0	1.8×10^{20}	7.5
Yingxiu-LMST (Hongkou)	5.0	8.4		
Beichuan-Pingtong (Beichuan)	8.4	6.0	9.4×10^{19}	7.3
Beichuan-Pingtong (Pingtong)	4.0	5.0		
Qingping	4.0	5.0	5.8×10^{19}	7.2
Qingchuan	4.0	0.0	4.3×10^{19}	7.1
Nanba	3.8	1.8	1.3×10^{19}	6.7

(d) trade-off of solutions between the Pengguan and Beichuan faults, resulting in greater error of slip estimates. The truth is perhaps a combination of these possible effects.

For the strike-slip component, our inverted surface slip offsets agree with field observations at Hongkou, Pingtong, and Nanba, but are greater than field observations at Longmen Shan Town, Gaochuan, and Beichuan (Fig. 7b). Our results are smaller than the field measurements at two spots, one is located ~15 km south of Hongkou, where our result of ~1 m slip is much less than a ~5 m offset reported by Lin *et al.* (2009); and another is on the Pengguan fault near Bailu, again our result of centimetre level slip is in large contrast with ~7.3 m offset reported by Lin *et al.* (2009). These two measurements by Lin *et al.* (2009), however, are not consistent with other field survey data, and may reflect not regional but rather localized deformation. The discrepancies between our results and the field geologic measurements from Longmen Shan Town to Beichuan could be due to distributed deformation across a finite width of the fault zone whose overall slip was not picked up completely by field geology.

Field studies discovered minor surface offset near Gaochuan, and envisioned that a right step of ~5 km on the Beichuan fault impeded rupture on the segment (Yu *et al.* 2010). Seismic studies also favoured minimum slip across this fault segment (Nishimura & Yagi 2008; Wang *et al.* 2008). Our results indeed reveal no significant thrust motion across the Gaochuan segment. However, we find 3–4 m right-lateral slip near the surface of the segment, which again could be due to distributed deformation across the fault zone that was not picked up by the field measurements.

5.2 Comparison of results with previous coseismic slip studies

Many slip distribution models have been published for the Wenchuan earthquake constrained using seismic and/or geodetic

data. Several recent studies supersede previous ones in most aspects with better data and/or models used. Here we compare our model and results with that of three representative studies, Shen *et al*. (2009), Wang *et al*. (2011), and Fielding *et al*. (2013).

This study uses the same GPS data set adopted by Wang *et al*. and Fielding *et al.* which is much denser and stronger than the one used by Shen *et al*. (2009), and greatly improves the resolution of the coseismic slip. This study also uses the ALOS PALSAR fine-beam interferogram data similar to that incorporated in Wang *et al.* and all the ALOS PALSAR fine-beam data and the Envisat data used by Fielding *et al*. Comparing to our previous study (Shen *et al.* 2009), the strengthened GPS and InSAR data help better constrain the static slip distribution, with improved resolution and better resolved slip concentrations along the fault rupture (Fig. 7). Fielding *et al*. also combined seismic data and solved for time-dependent rupture propagation; we make no such an effort in this study.

5.2.1 Elastic structure model

This study adopts two 1-D Earth structure models on either side of the Longmen Shan fault (Huang *et al.* 2003), which are markedly different from the uniform elastic half-space model used by Shen *et al*. (2009) and Wang *et al*. (2011) (Wang *et al*.'s trial to employ a layered model resulted in slightly worse model fitting to the data). Fielding *et al*. used a 1-D Earth elastic structure adopted from the CRUST2.0 model for both sides of the Longmen Shan fault (Supporting Information Fig. S2). We test a solution using the uniform half-space model, which yields a data fitting result with a reduced post-fit residual RMS of 2.059. The F-test of this model against our final model (with the reduced post-fit residual RMS as 1.936) confirms that the improvements of our final model over the uniform half-space model is significant at more than 99 per cent confidence. Our model reflects the large lateral contrast of the lithosphere structure across the Longmen Shan fault, which yields more accurate Green's functions for the inversion. Compared to the model assuming a layered structure for Green's function calculation, the one adopting a uniform elastic half-space yields a result of fault geometry with systematically steeper fault dip (about a couple of degrees near the surface) and deeper fault depth (∼2 km at mid depth) respectively. In this study we show that adopting a geologically more realistic model indeed leads to a better fit to the data, and the improvement of the modelling result is statistically significant.

5.2.2 Earthquake fault geometry

This study utilizes a listric fault in the model. Shen *et al*. (2009) and Fielding *et al*. assumed constant dip angles along depth for the fault segments, with a flat or a gentle dipping segment added at the downdip end of the southwest segment representing the downdip ramp of that segment. Wang *et al*. (2011) adopted a fault model with a ramp in the upper crust soling into a decollement in the lower crust. The Beichuan fault was divided into two large segments, the Beichuan and Qingchuan segments, and each had a single dip angle for the ramp and another dip angle for the decollement without lateral variation. Although Wang *et al*. conducted a systematic search to determine optimal values for the dip angles, their model could not account for the significant lateral variation of dip angle along strike of the Beichuan segment that were obtained in our result. Comparing the data post-fit residuals, our model yields better fitting to the near field data than the three previous studies, which we attribute mainly to better fault geometry and Earth structure models.

Wang *et al*.'s model adopted two straight lines as the surface trace of their meshed fault, ignoring the fault offsets near Hongkou and Beichuan. The fault model of Fielding *et al*. is similar to Wang *et al*. in its surface expression. Because the rupture surface traces have several offsets of as much as 5 km, ignoring their discontinuous geometry could result in significant biases in local slip estimation. One example is the fault model near Beichuan. Wang *et al*.'s fault slip model placed as much as 12.7 m peak slip at Beichuan, which is more than any of the field measurements and previous modelling results at the site, and likely biased due to placing the fault segment in their model 2 to 5 km northwestwards from its actual location.

Our model shows greater coseismic slip at the downdip extension of the SW segment (up to 3 m slip at ∼15 km depth and ∼20 km west of fault surface trace) than on all the other segments, which is quite consistent with all the previous models along this fault segment and depth range. About 1–2 m of slip on a near horizontal detachment fault at ∼20 km depth was found in previous studies (e.g. Shen *et al.* 2009); however, this could be affected by early post-seismic deformation during the first several days to months following the main shock. As we have no way to distinguish the contribution from early post-seismic deformation (several months or more from GPS and several days to months from InSAR), we choose not to include deformation sources located at >20 km depth. Although certain degree of uncertainty exists, what we have in our current model is arguably the most plausible coseismic slip model with the least aseismic slip contribution.

5.2.3 Model smoothing constraints

Wang *et al*. (2011) utilized smoothing constraints in their model inversion, which are more relaxed than that adopted in our model. As a result, their model features major slip maxima of ∼9 m dextral slip near Hongkou, Qingping, Beichuan, and Nanba, compared to ∼6, 4, 8 m, and ∼3.5 m dextral slip determined along the same fault sections in our model. Their slip estimates, therefore, are much greater than ours except at Beichuan, and such results are overall not supported by previous geological, seismological, and geodetic studies (e.g. Shen *et al.* 2009; Wang *et al.* 2009; Xu *et al.* 2009; Liu-Zeng *et al.* 2010; Nakamura *et al.* 2010; Tong *et al.* 2010).

5.3 Fault barrier model and its implication for earthquake rupture mechanics

Our result, together with most of the previous studies, shows that the slip distribution of the Wenchuan earthquake is complex. One of the explanations for this slip heterogeneity is that high peaks of slip represent 'asperities', which are strongholds along the fault due to rock mechanic properties (Burchfiel *et al.* 2008; Zhang *et al.* 2010) and/or fault surface morphology, which are capable of resisting more tectonic loading stress than their neighbourhood segments. Such a hypothesis, however, is hard to prove, since no good correlations can be found between the distribution of certain rock formations and locations of peak slip (e.g. Burchfiel *et al.* 2008). On the other hand, we note that locations of peak slip seem to correlate well with complexity of fault geometry. The Yingxiu-Hongkou peak slip zone spans two major branches of the Beichuan fault: in the southwest the Beichuan fault splits into two segments, with one sub-branch extending west then southwest to pass through Yingxiu city (Xu *et al.* 2009; see Fig. 1); and in the northeast the Xiaoyudong fault strikes perpendicular to the Beichuan fault and offsets the Beichuan fault by about 4 km (Liu-Zeng *et al.* 2009). The maximum slip resolved on this

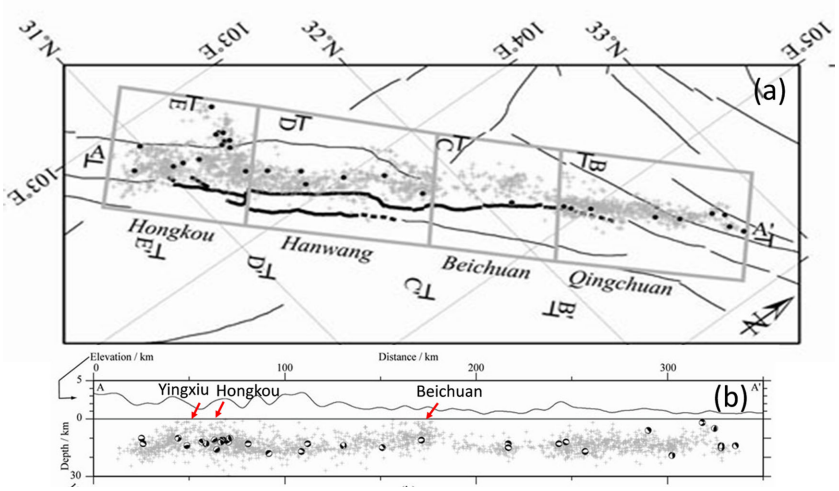

Figure 11. Aftershock distribution in (a) map view and (b) vertical cross-section view. Aftershock data set (including the focal mechanism solutions) is from Jiuhui Chen, which is the same as the one in Chen *et al*. (2009) with minor additions. Note the occurrence of aftershocks at shallow depth underneath Yingxiu-Hongkou and Beichuan.

stretch of the fault is located right on the fault junction with the Xiaoyudong fault. Near Beichuan city, peak slip resides on a segment of the fault that has several abrupt changes of its strike direction, and local offsets associated with such strike direction changes are about 0.5–1 km (Fig. 1). The geometric complexity near the peak slip at Nanba is also evident from this study, in that the fault dip angle changes abruptly by ~19° across this section of the Beichuan fault. The other two slip concentration regions on the Beichuan fault are located along the much straighter fault segments of Qingping and Qingchuan; their peak slips are less concentrated and release much less seismic moment than those near the Yingxiu-Hongkou and Beichuan concentrations.

Based on all of the observations we envision that the rupture process and slip distribution of the Wenchuan earthquake were determined mainly by fault geometry of the Beichuan fault. The geometric complexities along the fault represent barriers, which are harder to break than their neighbouring segments. In between large cascade ruptures, such as the Wenchuan earthquake, smaller events may have ruptured the straight, less-segmented sections, leading to a buildup of slip deficit across the step-overs and discontinuous geometric barriers. These sections would therefore have accumulated more tectonic loading stress prior to a large rupture. When one such barrier starts to break, the rupture could soon gain strong momentum from energy release around the barrier, and break cascade-style through a series of barriers along the fault. This proposed mechanism is similar to that of Duan & Oglesby (2005) who modelled multicycle dynamic ruptures of a strike-slip fault with along-fault changes in strike. With large rupture momentum accumulating along the path, such a cascade rupture could even propagate into the northeast segment of the Beichuan fault whose failure was very rare in the past based on palaeoseismologic evidence (Ran *et al.* 2010).

One notable exception to the inference above is the slip along the Gaochuan segment of the Beichuan fault, where the fault has a right step offset of ~5 km but experienced only 3–4 m coseismic slip which is smaller than the ~9.6 m slip to its northeast at Beichuan and ~6 m slip to its southwest at Qingping (Fig. 7). We attribute this exception to possible differences in fault strength and/or slip history. The Beichuan fault accommodates transpressional deformation with a dextral component. The fault materials would therefore undergo additional compressional stress if located within a left step, and extensional stress if located within a right step. Since brittle rocks are much weaker in tension than compression (Scholz 2002), the Gaochuan segment with a right step, might therefore represent a relatively weaker zone, and release tectonic stress through more frequent seismic events with smaller magnitudes. This notion agrees with Oglesby's (2005) finding that dilatational step-overs with linking normal faults are more prone to through-going rupture than compressional step-overs with linking thrust faults. The two most prominent left steps near Hongkou and Beichuan, on the other hand, would become strong geometric barriers, and not rupture until tectonic stress build-ups were very high, and finally rupture in a cascade failure mode.

The above interpretation of faulting process is supported by aftershock and deep drilling studies. Huang *et al*. (2008) and Chen *et al*. (2009), for example, showed that most of the precisely relocated Wenchuan aftershocks occurred in a depth range of 15–20 km, near the downdip edge of the coseismic rupture, suggesting full release of seismic moment across the brittle section of the seismogenic fault. Exceptions are found, however, in the regions near Yingxiu-Hongkou and Beichuan, where strong aftershock activity reached to shallow depth (Fig. 11). This observation reveals abundant secondary faulting after the main event at these step-overs, and the strong effect of fault geometry on the mechanical process around the fault system. Deep drilling of the Beichuan fault near Hongkou revealed that the fault interface is not narrow, but composed of a highly fractured deformation zone that is up to 120 metres thick (Wang *et al.* 2010). Such observations are consistent with our interpretation of failure of geometric complexities, which span a volume of material instead of a thin fault interface. The fault interface at Hongkou, although still a few kilometres away from the step-over, may be already affected by the buttressing effect due to mechanical deformation in the region, and become thickened. Such stronghold regions, therefore, acquired their mechanic strength mainly due to their geometric complexity, not rock or fault rheologic properties, thus we refer to them as geometric barriers, not asperities, to distinguish their mechanic differences.

5.4 Deformation mechanism of eastern Tibet

It has been debated what drives deformation of eastern Tibet, particularly along its eastern margin, the Longmen Shan orogenic belt and fault system. Has the Longmen Shan system been pushed up mainly by the lower crust flow of the Tibet (e.g. Royden *et al.* 1997, 2008; Clark & Royden 2000), or by brittle crustal thickening and shortening (e.g. Hubbard & Shaw 2009)? To address this problem our modelling results may provide some clue. Our results support a listric fault geometry, whose dip angle ranges from 36° to 45° at the surface for the southern segment of the fault, and flattened to 26°–32° at 20 km depth (the result loses depth resolution for the shallow dipping segment of the listric fault further to the west). Such a fault geometry is consistent with seismic reflection studies across the Longmen Shan fault system (Jia *et al.* 2006, 2010; Li *et al.* 2010; Wang *et al.* 2013, 2014a; Feng *et al.* 2016), which show a ramp structure dipping to the west. The fault system seems to connect to a decollement in the mid crust, illuminated as reflectors in seismic reflection data (e.g. Guo *et al.* 2013) and as a velocity gradient layer in receiver function (e.g. Zhang *et al.* 2009b; Liu *et al.* 2014) studies. GPS observations spanning the Wenchuan earthquake confirm slip on the detachment fault either coseismically or post-seismically (Wang *et al.* 2011). Such a kinematic model agrees with the model of Hubbard & Shaw (2009) and Hubbard *et al*. (2010) for crustal shortening through reverse faulting and folding in the upper crust above a decollement layer in the mid crust. This fault kinematic model differs from the lower crust flow model (e.g. Royden *et al.* 2008) as it supports that the orogeny of the Longmen Shan is driven mainly by the lateral push and reverse faulting in the upper crust, not by the upwelling of the viscous flow from the lower crust. The lower crustal flow, if it exists, would demand the lower crust materials move eastward faster than the upper crust (e.g. Royden *et al.* 2008). What has been inferred from geodetic observations after the quake, to the contrary however, is that the upper crust moved eastward faster than the lower crust across the detachment fault (at least for the coseismic/post-seismic time period). We therefore envision a model that responding to horizontal compression, the upper and lower crust are being thickened with different mechanisms: the upper crust deforms by brittle thrust and reverse faulting, and the lower crust by continuous viscous deformation. The decollement system located in the mid crust, with lower friction or viscosity than its ambient media (due to various strain weakening mechanisms commonly found in shear zones, grain size reduction, fluid effects, shear heating, etc.), decouples the two deformation modes.

Our decoupled crust deformation model also agrees with the interseismic model proposed by Thompson *et al*. (2015), in which a detachment fault exists in the mid crust to separate long term deformation between the upper and lower crust. Our model, however, does not agree with Thompson *et al*. for their assertion that the detachment fault extending between the Longmen Shan and Longriba faults, is locked interseismically. Seismic reflection and receiver function studies (Zhang *et al.* 2009b; Guo *et al.* 2013) show that the detachment fault is located at 24–30 km depth southeast of the Longriba fault, and continental crust would be more likely to be ductile than brittle at this depth range (Huang *et al.* 2014). Wang *et al*. (2011) observed 10–40 cm displacements either coseismically or post-seismically for sites located 50–120 km northwest of the Beichuan fault. Post-earthquake observations at these mid to far field sites were made several months to almost a year after the quake, leaving plenty time for post-seismic deformation to accumulate (Wang *et al.* 2011). Early GPS post-seismic observations recorded several centimetre displacements in the hanging wall (fig. S1 in Supplementary Materials of Shen *et al.* 2009; Ding *et al.* 2013). Such observations are smaller than the 10–40 cm displacements observed by Wang *et al*. (2011), but the difference could be due to missing post-seismic deformation of later phase for observations of the very early phase, taking place during the first several weeks following the quake prior to the GPS site deployment (Shen *et al.* 2009; Ding *et al.* 2013). Such an argument is supported by aftershock observations (Chen *et al.* 2009; An *et al.* 2010). If the detachment fault was ruptured coseismically, aftershocks would be expected to highlight the fault rupture; however, very few aftershocks were observed northwest of and more than 50 km away from the Beichuan fault, none of which occurred below 20 km depth. We conclude that the detachment fault has to be creeping, at least intermittently during the interseismic time period, and acts as a decoupling layer to separate deformation of the upper and lower crust.

6 CONCLUSIONS

Using a composite geodetic data set we have inverted for fault geometry and slip distribution of the Wenchuan earthquake. Our results show that adopting layered earth structure models on both sides of the Beichuan fault significantly improved data fitting over a uniform half-space structure model.

The results also reveal that the Beichuan fault that ruptured in the Wenchuan earthquake is listric in shape, with varying fault dip angle along strike. The dip angle near the surface is ∼36° at the south end of the Yingxiu-Hongkou segment of the fault, changes to 43°, 67°, and 51° at Hongkou, Qingping, and Beichuan, becomes ∼51° south of Nanba, jumps to 70° north of the Nanba junction, and reaches ∼83° on the Qingchuan segment of the fault. Near the base of the coseismic rupture the fault dip shallows to about as little as 26°. The rupture style of the Wenchuan earthquake changes from predominantly thrust at the southwest end to dextral at the northeast end of the fault rupture.

The coseismic slip along the discontinuous rupture zone was very heterogeneous featuring multiple slip maxima. The maximum slips are located around Yingxiu-Hongkou and Beichuan, where the faults show bifurcation and abrupt change in fault strike direction. Such geometric complexities are interpreted as geometric barriers for rupture propagation, and their failures should be rare, and likely occur during a cascade rupture such as the Wenchuan earthquake. The fault slip peaks near the surface for most parts of the fault, with ∼8.4 m thrust and ∼5 m dextral slip near Hongkou, ∼6 m thrust and ∼8.4 m dextral slip near Beichuan, ∼4 m thrust and ∼5.0 m dextral slip near Pingtong, ∼4 m dextral slip near Qingchuan, and ∼2 m thrust and ∼4 m dextral slip near Nanba, respectively. Slip on the Pengguan fault is dominated by thrust faulting, with 1–2 m of slip over most part of the fault plane. The seismic moment released by the rupture above 20 km depth is 8.2×10^{21} N m, corresponding to a M_w7.9 event. The seismic moments released on the local slip concentrations are equivalent to events of M_w7.5 at Yingxiu-Hongkou, M_w7.3 at Beichuan-Pingtong, M_w7.2 near Qingping, M_w7.1 near Qingchuan, and M_w6.7 near Nanba, respectively, contributing to strong ground shaking and structure destruction in these regions (Wen *et al.* 2010).

The fault geometry and kinematics agree with a model in which crustal deformation at the eastern margin of the Tibetan plateau is decoupled by differential motion across a decollement in the mid crust, above which the deformation is dominated by brittle thrust

and reverse faulting and below which viscous horizontal shortening and vertical thickening occur.

ACKNOWLEDGEMENTS

We thank the Editor for handling of the manuscript, and two anonymous reviewers for their thoughtful and constructive comments. We are also grateful to Eric Fielding for providing part of the InSAR interferograms used in this study. Special thanks are to the survey teams of the China Earthquake Administration and Sichuan Bureau of the National Administration of Surveying, Mapping and Geoinformation of China, for GPS data collection under exceptionally harsh survey conditions. Jiuhui Chen provided the Wenchuan aftershock data set used in Fig. 11. This research was supported by the National Science Foundation of China (41090294, 41674055). It was also supported by NSF grants (EAR-0911762) for Z-KS and (EAR-1014880) for RB.

REFERENCES

An, M., Feng, M. & Long, C., 2010. Deep ruptures around the hypocenter of the 12 May 2008 Wenchuan earthquake deduced from aftershocks observations, *Tectonophysics,* **491,** 96–104.

Bassin, C., Laske, G. & Masters, G., 2000. The current limits of resolution for surface wave tomography in North America, *EOS, Trans. Am. geophys. Un.,* **81,** F897.

Burchfiel, B.C., Chen, Z., Liu, Y. & Royden, L.H., 1995. Tectonics of the Longmen Shan and adjacent regions, *Int. Geol. Rev.,* **37,** 661–735.

Burchfiel, B.C. *et al.*, 2008. A geological and geophysical context for the Wenchuan earthquake of 12 May 2008, Sichuan, People's Republic of China, *GSA Today,* **18,** 4–11.

Chen, J.H., Liu, Q.Y., Li, S.C., Guo, B., Li, Y., Wang, J. & Qi, S.H., 2009. Seismotectonic study by relocation of the Wenchuan M_S8.0 earthquake sequence, *Chin. J. Geophys.,* **52**(2), 390–397 (in Chinese with English abstract).

Clark, M. & Royden, L., 2000. Topographic ooze: building the eastern margin of Tibet by lower crustal flow, *Geology,* **28**(8), 703–706.

Densmore, A.L., Ellis, M.A., Li, Y., Zhou, R., Hancock, G.S. & Richardson, N., 2007. Active tectonics of the Beichuan and Pengguan faults at the eastern margin of the Tibetan Plateau, *Tectonics,* **26,** TC4005, doi:10.1029/2006TC001987.

Densmore, A.L., Li, Y., Richardson, N.J., Zhou, R., Ellis, M. & Zhang, Y., 2010. The role of late quaternary upper-crustal faults in the 12 May 2008 Wenchuan earthquake, *Bull. seism. Soc. Am.,* **100,** 2700–2712.

Ding, K., Xu, C. & Wen, Y., 2013. Postseismic deformation associated with the 2008 Wenchuan earthquake by GPS data, *Geomatics Inf. Sci. Wuhan Univ.,* **38,** 131–135 (in Chinese with English abstract).

Du, Y. & Segall, P. &,Gao, H., 1994. Dislocations in inhomogeneous media via a moduli perturbation approach: general formulation and two-dimensional solutions, *J. geophys. Res.,* **99**(B7), 13 767–13 779.

Duan, B. & Oglesby, D.D., 2005. Multicycle dynamics of nonplanar strike-slip faults, *J. geophys. Res.,* **110,** B03304, doi:10.1029/2004JB003298.

Feng, G., Hetland, E.A., Ding, X., Li, Z. & Zhang, L., 2010. Coseismic fault slip of the 2008 M_w 7.9 Wenchuan earthquake estimated from InSAR and GPS measurements, *Geophys. Res. Lett.,* **37,** L01302, doi:10.1029/2009GL041213.

Feng, S.Y. *et al.*, 2016. Deep crustal deformation of the Longmen Shan, eastern margin of the Tibetan Plateau, from seismic reflection survey and Finite Element modeling, *J. geophys. Res.,* **121,** doi:10.1002/2015JB012352.

Fielding, E.J., Sladen, A., Li, Z., Avouac, J.-P., Bürgmann, R. & Ryder, I., 2013. Kinematic fault slip evolution source models of the 2008 M7.9 Wenchuan earthquake in China from SAR interferometry, GPS and teleseismic analysis and implications for Longmen Shan tectonics, *Geophys. J. Int.,* **194**(2), 1138–1166.

Furuya, M., Kobayashi, T., Takada, Y. & Murakami, M., 2010. Fault source modeling of the 2008 Wenchuan earthquake based on ALOS/PALSAR data, *Bull seism. Soc Am.,* **100,** 2750–2766.

Guo, X., Gao, R., Keller, G., Xu, X., Wang, H. & Li, W., 2013. Imaging the crustal structure beneath the eastern Tibetan Plateau and implications for the uplift of the Longmen Shan range, *Earth planet. Sci. Lett.,* **379,** 72–80.

Hao, K.X., Si, H., Fujiwara, H. & Ozawa, T., 2009. Coseismic surface-ruptures and crustal deformations of the 2008 Wenchuan earthquake M_w7.9, China, *Geophys. Res. Lett.,* **36,** L11303, doi:10.1029/2009GL037971.

Hashimoto, M., Enomoto, M. & Fukushima, Y., 2009. Coseismic deformation from the 2008 Wenchuan, China, earthquake derived from ALOS/PALSAR Images, *Tectonophysics,* **491,** 59–71.

Hearn, E.H. & Bürgmann, R., 2005. The effect of elastic layering on inversions of GPS data for coseismic slip and resulting stress changes: strike-slip earthquakes. *Bull. seism. Soc. Am.,* **95**(5), 1637–1653.

Huang, M.H., Bürgmann, R. & Freed, A.M., 2014. Probing the lithospheric rheology across the eastern margin of the Tibetan Plateau, *Earth planet. Sci. Lett.,* **396,** 88–96.

Huang, Y., Wu, J.P., Zhang, T.Z. & Zhang, D.N., 2008. Relocation of the M8.0 Wenchuan earthquake and its aftershock sequence, *Sci. China D,* **51**(12), 1703–1711.

Huang, Z., Su, W., Peng, Y., Zheng, Y. & Li, H., 2003. Rayleigh wave tomography of China and adjacent regions, *J. geophys. Res.,* **108,** 2073, doi:10.1029/2001JB001696.

Hubbard, J. & Shaw, J., 2009. Uplift of the Longmen Shan and Tibeten plateau, and the 2008 Wenchuan (M7.9) earthquake, *Nature,* **458,** 194–197.

Hubbard, J., Shaw, J.H. & Klinger, Y., 2010. Structural setting of the 2008 M_w 7.9 Wenchuan, China, earthquake, *Bull. seism. Soc. Am.,* **100**(5B), 2713–2735.

Jackson, D.D. & Matsu'ura, M., 1985. A Bayesian approach to nonlinear inversion, *J. geophys. Res.,* **90,** 581–591.

Ji, C. & Hayes, G., 2008. 'Preliminary result of the May 12, 2008 M_w 7.9 eastern Sichuan, China earthquake'. Available at: http://earthquake.usgs.gov/eqcenter/eqinthenews/2008/ us2008ryan/finite_fault.php, last accessed 11 October 2013.

Jia, D., Wei, G.Q., Chen, Z.X., Li, B.L., Zeng, Q. & Yang, G., 2006. Longmen Shan fold-thrust belt and its relation to the western Sichuan basin in central China: new insights from hydrocarbon exploration, *AAPG Bull.,* **90**(9), 1425–1447.

Jia, D. *et al.*, 2010. Structural model of 2008 M_w 7.9 Wenchuan earthquake in the rejuvenated Longmen Shan thrust belt, China, *Tectonophysics,* **491,** 174–184.

Jiang, Z., Wang, M., Wang, Y.Z. & Li, Q., 2014. GPS constrained coseismic source and slip distribution of the 2013 M_w6.6 Lushan, China, earthquake and its tectonic implications, *Geophys. Res. Lett.,* **41,** doi:10.1002/2013GL058812.

Klinger, Y., Ji, C., Shen, Z.-K. & Bakun, W.H., 2010. Introduction to the special issue on the 2008 Wenchuan, China, earthquake, *Bull. seism. Soc. Am.,* **100,** 2353–2356.

Li, Y. *et al.*, 2010. Structural interpretation of the coseismic faults of the Wenchuan earthquake: three-dimensional modeling of the Longmen Shan fold-and-thrust belt, *J. geophys. Res.,* **115,** B04317, doi:10.1029/2009JB006824.

Lin, A., Ren, Z.K., Jia, D. & Wu, X.J., 2009. Co-seismic thrusting rupture and slip distribution produced by the 2008 M 7.9 Wenchuan earthquake, China, *Tectonophysics,* **471,** 203–215.

Liu, Q.Y., Li, Y., Chen, J.H., Guo, B., Li, S., Wang, J., Zhang, X. & Qi, S., 2009. Wenchuan M8.0 earthquake: preliminary study of the S-wave velocity structure of the crust and upper mantle, *Chin. J. Geophys.,* **52**(2), 309–319 (in Chinese with English abstract).

Liu, Q.Y., Van der Hilst, R.D., Li, Y., Yao, H.J., Chen, J.H., Guo, B., Qi, S.H., Wang, J., Huang, H. & Li, S.C., 2014. Eastward expansion of the Tibetan Plateau by crustal flow and strain partitioning across faults, *Nat. Geosci.,* **7**(5), 361–365.

Liu-Zeng, J. *et al.*, 2009. Co-seismic ruptures of the 12 May 2008, Ms 8.0 Wenchuan earthquake, Sichuan: east-west crustal shortening on oblique, parallel thrusts along the eastern edge of Tibet, *Earth planet. Sci. Lett.,* **286**(3–4), 355–370.

Liu-Zeng, J., Wen, L., Sun, J., Zhang, Z., Hu, G., Xing, X., Zeng, L. & Xu, Q., 2010. Surficial slip and rupture geometry on the Beichuan fault near Hongkou during the M_w 7.9 Wenchuan earthquake, China, *Bull. seism. Soc. Am.,* **100**(5B), 2615–2650.

Nakamura, T., Tsuboi, S., Kaneda, Y. & Yamanaka, Y., 2010. Rupture process of the 2008 Wenchuan, China earthquake inferred from teleseismic waveform inversion and forward modeling of broadband seismic waves, *Tectonophysics,* **491,** 72–84.

Nishimura, N. & Yagi, Y., 2008. 'Rupture process for May 12, 2008 Sichuan earthquake (preliminary result)'. Available at: http://www.geol.tsukuba.ac.jp/~nisimura/20080512/, last accessed 11 October 2013.

Oglesby, D.D., 2005. The dynamics of strike-slip step-overs with linking dip-slip faults, *Bull. seism. Soc. Am.,* **95,** 1604–1622.

Parsons, T., Ji, C. & Kirby, E., 2008. Stress changes from the 2008 Wenchuan earthquake and increased hazard in the Sichuan basin, *Nature,* **454,** 509–510.

Parsons, T. & Segou, M., 2014. Stress, distance, magnitude, and clustering influences on the success or failure of an aftershock forecast: the 2013 M 6.6 Lushan earthquake and other examples, *Seismol. Res. Lett.,* **85**(1), 44–51.

Ran, Y.K. *et al.*, 2010. Paleoseismic evidence and repeat time of large earthquakes at three sites along the Longmenshan fault zone, *Tectonophysics,* **491,** 141–153.

Royden, L.H., Burchfiel, B.C., King, R.W., Wang, E., Chen, Z.L., Shen, F. & Liu, Y.P., 1997. Surface deformation and lower crustal flow in eastern Tibet, *Science,* **294,** 1671–1677.

Royden, L.H., Burchfiel, B.C. & Van der Hilst, R.D., 2008. The geological evolution of the Tibetan plateau, *Science,* **321,** 1054–1058.

Savage, J.C., 1987. Effect of crustal layering upon dislocation modeling, *J. geophys. Res.,* **92**(B10), 10 595–10 600.

Scholz, C., 2002. *Mechanics of Earthquakes and Faulting*, Cambridge Univ. Press.

Shen, Z.-K., Ge, B.X., Jackson, D.D., Potter, D., Cline, M. & Sung, L., 1996. Northridge earthquake rupture model based on Global Positioning System measurements, *Bull. seism. Soc. Am.,* **86**(1B), 37–48.

Shen, Z.-K., Lü, J.N., Wang, M. & Bürgmann, R., 2005. Contemporary crustal deformation around the southeast borderland of the Tibetan Plateau, *J. geophys. Res.,* **110,** B11409, doi: 10.1029/2004jb003421.

Shen, Z.-K. *et al.*, 2009. Slip maxima at fault junctions and rupturing of barriers during the 2008 Wenchuan earthquake, *Nat. Geosci.,* **2,** 718–724.

Tao, W., Hu, C.B., Wan, Y.G., Shen, Z.-K. & Wang, K., 2011. Dynamic modeling of thrust earthquake on listric fault and its inference to study of Wenchuan earthquake, *Chin. J. Geophys,* **54**(5), 1260–1269 (in Chinese with English abstract).

Thompson, T.B., Plesch, A., Shaw, J.H. & Meade, B.J., 2015. Rapid slip-deficit rates at the eastern margin of the Tibetan Plateau prior to the 2008 M_w 7.9 Wenchuan earthquake, *Geophys. Res. Lett.,* **42**(6), 1677–1684.

Toda, S., Lin, J., Meghraoui, M. & Stein, R.S., 2008. 12 May 2008 M=7.9 Wenchuan, China, earthquake calculated to increase failure stress and seismicity rate on three major fault systems, *Geophys. Res. Lett.,* **35,** L17305, doi:10.1029/2008GL034903.

Tong, X., Sandwell, D.T. & Fialko, Y., 2010. Coseismic slip model of the 2008 Wenchuan earthquake derived from joint inversion of interferometric synthetic aperture radar, GPS, and field data, *J. geophys. Res.,* **115,** B04314, doi:10.1029/2009JB006625.

Wald, D.J. & Graves, R.W., 2001. Resolution analysis of finite fault source inversion using one- and three-dimensional Green's functions 2. Combining seismic and geodetic data, *J. geophys. Res.,* **106**(B5), 8767–8788.

Wan, Y. & Shen, Z.-K. 2010. Coulomb failure stress changes on faults caused by the 2008 M_w7.9 Wenchuan earthquake, China, *Tectonophysics,* **491,** 105–118.

Wang, R., Martin, L. & Roth, F., 2006. PSGRN/PSCMP–a new code for calculating co- and post-seismic deformation, geoid and gravity changes based on the viscoelastic-gravitational dislocation theory, *Comput. Geosci.,* **32,** 527–541.

Wang, C.-Y., Han, W.-B., Wu, J.-P., Lou, H. & Chan, W.W., 2007. Crustal structure beneath the eastern margin of theTibetan Plateau and its tectonic implications, *J. geophys. Res.,* **112,** B07307, doi:10.1029/2005JB003873.

Wang, W.M., Zhao, L.F., Li, J. & Yao, Z.X., 2008. Rupture process of the Ms 8.0 Wenchuan earthquake of Sichuan, China, *Chin. J. Geophys.,* **51**(5), 1403–1410 (in Chinese with English abstract).

Wang, Q., Cui, D., Zhang, X., Wang, W., Liu, J. & Tian, K., 2009. Coseismic vertical deformation of the Ms8.0 Wenchuan earthquake from repeated levelings and its constraint on listric fault geometry, *Earthq. Sci.,* **22,** 595–602.

Wang, H., Li, H., Pei, J., Li, T., Huang, Y. & Zhao, Z., 2010. Structural and lithologic characteristics of the Wenchuan earthquake fault zone and its relationship with the seismic activity, *Quat. Sci.,* **30**(4), 768–778 (in Chinese with English abstract).

Wang, Q. *et al.*, 2011. Rupture of deep faults in the 2008 Wenchuan earthquake and uplift of the Longmen Shan, *Nat. Geosci.,* **4,** 634–640.

Wang, M., Jia, D., Shaw, J.H., Hubbard, J., Lin, A., Li, Y. & Shen, L., 2013. Active fault-related folding beneath an alluvial terrace in the southern Longmen Shan Range Front, Sichuan basin, China: implications for seismic hazard, *Bull. seism. Soc. Am.,* **103**(4), 2369–2385.

Wang, M., Jia, D., Shaw, J.H., Hubbard, J., Plesch, A., Li, Y. & Liu, B., 2014a. The 2013 Lushan earthquake: implications for seismic hazards posed by the Range Front blind thrust in the Sichuan Basin, China, *Geology,* **42**(10), 915–918.

Wang, Y., Wang, F., Wang, M., Shen, Z.-K. & Wan, Y., 2014b. Coulomb stress change and evolution induced by the 2008 Wenchuan earthquake and its delayed triggering of the 2013 M_w 6.6 Lushan earthquake, *Seismol. Res. Lett.,* **85**(1), 52–59.

Williams, C.A. & Wallace, L.M., 2015. Effects of material property variations on slip estimates for subduction interface slow-slip events, *Geophys. Res. Lett.,* **42,** 1113–1121.

Wen, Z., Xie, J., Gao, M., Hu, Y. & Chau, K.T., 2010. Near-source strong ground motion characteristics of the 2008 Wenchuan earthquake, *Bull. seism. Soc. Am.,* **100**(5B), 2425–2439.

Working Group of the Crustal Motion Observation Network of China Project, 2008. The coseismic displacement of 2008 Wenchuan Ms8.0 earthquake measured by GPS, *Sci. China D,* **38**(10), 1195–1206 (in Chinese with English abstract).

Xu, C., Liu, Y., Wen, Y. & Wang, R., 2010. Coseismic slip distribution of the 2008 M_w7.9 Wenchuan earthquake from joint inversion of GPS and InSAR data, *Bull. seism. Soc. Am.,* **100,** 2736–2749.

Xu, X. *et al.*, 2008. The Ms8.0 Wenchuan earthquake surface ruptures and its seismogenic structure, *Seismol. Geol.,* **30**(3), 597–629 (in Chinese with English abstract).

Xu, X., Wen, X., Yu, G., Chen, G., Klinger, Y., Hubbard, J. & Shaw, J., 2009. Coseismic reverse- and oblique-slip surface faulting generated by the 2008 M_w 7.9 Wenchuan earthquake, China, *Geology,* **37,** 515–518.

Xu, Z.J. & Song, X., 2010. Joint inversion for crustal and Pn velocities and Moho depth in Eastern Margin of the Tibetan Plateau, *Tectonophysics,* **491**(1–4), 185–193.

Yao, H., Beghein, C. & van der Hilst, R.D., 2008. Surface wave array tomography in SE Tibet from ambient seismic noise and two-station analysis—II: Crustal and upper-mantle structure, *Geophys. J. Int.,* **173,** 205–219.

Yu, G. *et al.*, 2010. Fault-Scarp features and cascading-rupture model for the M_w7.9 Wenchuan earthquake, eastern Tibetan plateau, China, *Bull. seism. Soc. Am.,* **100,** 2590–2614.

Zhang, P.-Z., Shen, Z.-K., Wang, M., Gan, W.J., Bürgmann, R. & Molnar, P., 2004. Continuous deformation of the Tibetan Plateau from global positioning system data, *Geology,* **32,** 809–812.

Zhang, Y., Feng, W.P., Xu, L.S., Zhou, C.H. & Chen, Y.T., 2009a. Spatio-temporal rupture process of the 2008 great Wenchuan earthquake, *Sci. China D,* **52**(2), 145–154.

Zhang, Z., Wang, Y., Chen, Y., Houseman, G.A., Tian, X., Wang, E. & Teng, J., 2009b. Crustal structure across Longmenshan fault belt from

passive source seismic profiling, *Geophys. Res. Lett.,* **36**(17), L17, 310, doi:10.1029/2009GL039580.

Zhang, P.-Z., Wen, X., Shen, Z.-K. & Chen, J., 2010. Oblique, high-angle, listric-reverse faulting and associated development of strain: the Wenchuan earthquake of May 12, 2008, Sichuan, China, *Annu. Rev. Earth planet. Sci.,* **38,** 351–380.

Zhang, G., Qu, C., Shan, X., Song, X., Zhang, G., Wang, C., Hu, J.-C. & Wang, R., 2011. Slip distribution of the 2008 Wenchuan Ms 7.9 earthquake by joint inversion from GPS and InSAR measurements: a resolution test study, *Geophys. J. Int.,* **186,** 207–220.

Zhu, A.L., Xu, X.W., Diao, G.L., Su, J.R., Feng, X.D., Sun, Q. & Wang, J.L., 2008. Relocation of the Ms8.0 Wenchuan earthquake sequence in part: preliminary seismotectonic analysis, *Seismol. Geol.,* **30**(3), 759–767 (in Chinese with English abstract).

SUPPORTING INFORMATION

Supplementary data are available at *GJIRAS* online.

Figure S1. Downsampled data used in this study. Original data are shown in Fig. 2.

Figure S2. Comparison of Earth structure models of Huang *et al*. (2003), Wang *et al*. (2007) and Liu *et al.* (2009), and CRUST2.0 used by Fielding *et al*. (2013). (a) Shear modulus, (b) Young's modulus and (c) density depth profiles. SB: Sichuan Basin, ET: Eastern Tibet.

Table S1. Fault slip model.

Table S2. GPS and triangulation horizontal data fitting.

Table S3. GPS and levelling vertical data fitting.

Table S4. InSAR LOS downsampled data and modelling fitting.